Nuclide cross-sections of fission fragments in the reaction 208Pb + p at 500 A MeV

B. Fernández-Domínguez, P. Armbruster, L. Audouin, J. Benlliure, M. Bernas, A. Boudard, E. Casarejos, S. Czajkowski, J.E. Ducret, T. Enqvist, et al.

Nuclide cross-sections of fission fragments in the reaction $^{208}Pb + p$ at 500 A MeV.

B. Fernández-Domínguez[1, a] P. Armbruster[b] L. Audouin[c]
J. Benlliure[d] M. Bernas[c] A. Boudard[a] E. Casarejos[d]
S. Czajkowski[e] J.E. Ducret[a] T. Enqvist[b] B. Jurado[b]
R. Legrain[2, a] S. Leray[a] B. Mustapha[c] J. Pereira[d]
M. Pravikoff[e] F. Rejmund[b,c] M.V. Ricciardi[b] K.-H. Schmidt[b]
C. Stéphan[c] J. Taieb[b,c] L. Tassan-Got[c] C. Volant[3, a]
W. Wlazlo[a]

[a] *DAPNIA/SPhN CEA/Saclay, F-91191 Gif sur Yvette Cedex, France*
[b] *GSI, Planckstrasse 1, 64291 Darmstadt, Germany*
[c] *IPN Orsay, F-91406 Orsay Cedex, France*
[d] *Univ. de Santiago de Compostela, E-15706 Santiago de Compostela, Spain*
[e] *CENBG, F-33175 Gradignan Cedex, France*

Abstract

The isotopic distributions and recoil velocities of the fission fragments produced in the spallation reaction $^{208}Pb + p$ at 500 A MeV have been measured using the inverse-kinematics technique, a lead beam onto a liquid-hydrogen target, and the high-resolution spectrometer FRS at GSI. The shapes of the different distributions are found in good agreement with previously published data while the deduced total fission cross-section is higher than expected from existing systematics and some previous measurements. From the experimental data, the characteristics of the average fissioning system can be reconstructed in charge, mass and excitation energy, and the average number of post-fission neutrons can be inferred. The results are also compared to different models describing the spallation reaction. The intranuclear cascade code INCL4 followed by the de-excitation code ABLA is shown to describe reasonably well the evolution of the isotopic distribution shapes between 500 and 1000 A MeV.

Key words: spallation reaction, nuclei identification, production of fission fragments, recoil velocities, accelerator-driven systems, spallation sources.

1 Introduction

Since several years a large effort has been devoted at GSI to the measurements of evaporation residues and fission fragments in spallation reactions induced by proton and deuteron on gold [1, 2], lead [3, 4, 5] and uranium [6, 7]. The primary trigger for these new measurements was the need for precise spallation data which were required by various ambitious projects like neutron spallation sources [8, 9] and accelerator-driven systems (ADS) for incineration of nuclear waste [10, 11, 12]. Further applications were also foreseen like the production of radioactive beams [13]. More traditional was also the astrophysical interest for the spallation reactions on hydrogen, which is the major reaction in the interstellar matter encountered by the cosmic rays during their flights [14].

The present experimental technique allows the full identification in mass and charge of all products of the spallation reaction thanks to a magnetic separation and the use of the inverse kinematics. It employs the high-energy heavy-ion beams, delivered by the SIS synchrotron at GSI Darmstadt, impinging on a liquid-hydrogen target and the high-resolution FRS spectrometer equipped with detectors for energy-loss and time-of-flight measurements. This allows the detection of the primary products before any radioactive decay (lifetime greater than $\sim$300 ns) and gives also access to their kinematical properties, in contrast to experiments in which a target is irradiated in direct kinematics and the residues detected by mass or γ-spectrometry [15, 16]. In the latter case, it is easy to measure excitation functions but the measurements are restricted to a few residues and very often give access to cumulative cross-sections only.

Our previous measurements with heavy beams were mainly performed at 1000 A MeV, which corresponds to the incident energy foreseen for most of the spallation target projects. However, the interest for the evolution with the bombarding energy of the residue production yields is quite clear: in thick targets, the incident beam is slowed down, and the primary reactions can occur from the incident energy down to low energies. Furthermore, there are also some projects at lower energies aiming at demonstrating the different components of ADS as MEGAPIE [17] or MYRRHA [18]. It is the purpose of the present work to extend our set of data on lead towards lower energies. Actually, for heavy beams as lead, our experimental method cannot be applied at too low energies and already at the chosen 500 A MeV bombarding energy, specific experimental difficulties occur, which were not existing at 1000 A MeV, like larger angular or ionic-charge state dispersions.

The understanding of the spallation reaction mechanism is also of great inter-

[1] This work forms part of the PhD thesis of B. Fernández-Domínguez
[2] Deceased.
[3] Corresponding author: cvolant@cea.fr

est since it is out of the experimentalist possibilities to measure all the data needed for the design of any application. For that, simulations are required and the nuclear models that enter the simulation codes need to be checked and/or tuned on a data base as large as reasonable. Experiments enabling a detailed understanding of the mechanism and involving various target elements and bombarding energies are thus required for this purpose. As shown in [1, 3, 4, 7], the measurement of the complete isotopic and velocity distributions really allows to test the models and no such data were existing around 500 MeV.

Since their discovery, the spallation reactions have been modeled in two stages [19]. During the first one, the intranuclear-cascade (INC) step, the incident proton interacts with the nucleons of the target nucleus leading to an excited prefragment. In the second step, the prefragment can de-excite by evaporation of light particles and/or fission. Old models are still currently used in the high-energy transport codes employed for applications. However, recently, new ones still under development have been implemented into some of the transport codes. Among the new developments, one could cite as examples recent INC [20, 21, 22] as well as evaporation-fission models [23, 24, 25]. Some other models consider also an intermediate, preequilibrium stage between the fast intranuclear cascade stage and the slow evaporation/fission stage (see for example [26] and references therein). The aim of the present work is also to provide new tests of some of the codes devoted to the spallation-reaction modeling. In this paper, we deal only with the fission fragments emitted in the $^{208}Pb + p$ reaction at 500 A MeV, the evaporation residues being the subject of a forthcoming publication [27]. This implies that the model for the second stage is of particular interest. Actually, large efforts towards the improvement of the fission process treatment have been done in the model developed at GSI [23] by introducing physical aspects which are omitted in most of the evaporation-fission codes. Nevertheless, there is a delicate interplay between these models and the INC codes which deliver the inputs to the second stage like initial mass, charge, excitation energy and angular-momentum distributions. Actually, it will be shown that the properties of the fissioning system can be reconstructed, providing in fact a test of the INC stage as well.

In section 2, we describe the experimental setup and the analysis procedure used to obtain the full identification of the fission products for all elements from Z=23 to Z=56. Details will be given on the various corrections needed to obtain the final isotopic cross-sections and velocity distributions. The results and the comparisons with data obtained from direct-kinematics measurements will be discussed in the following section. Section 4 will be devoted to the reconstruction of the average fissioning system, which also allows to estimate the average number of neutrons evaporated post-fission. Finally, in the last section, the various measured observables will be confronted to different models used for describing the spallation reactions.

2 Experimental procedure

The experiment has been performed at the GSI (Darmstadt) facility. The inverse-kinematics technique, i.e. a lead beam onto a liquid-hydrogen target, has been employed in combination with the in-flight spectrometer, FRS (FRagment Separator) to measure the residual nuclide production in the spallation reaction. This technique enables the identification of each nuclide as well as the measurement of its kinematical properties before radioactive decays.

A detailed description of the experimental set-up and the analysis method can be found in previous publications [1, 4, 7]. Therefore we just recall here the detection principle and point out the specificities and difficulties related to the experiment at 500 A MeV. In the present work only fragments with a charge higher than 20 were studied.

2.1 Experimental set-up.

The FRagment Separator FRS [28], [29] is a zero-degree spectrometer made of four dipoles having a deflection angle of 30 degrees with a dispersive intermediate image plane (S2) and an achromatic final image plane (S4). A schematic view of the FRS with the specific equipment used in this experiment is shown in Fig.1. The angular and momentum acceptances around the central trajectory are ±15 mrad and ±1.5 %, respectively.

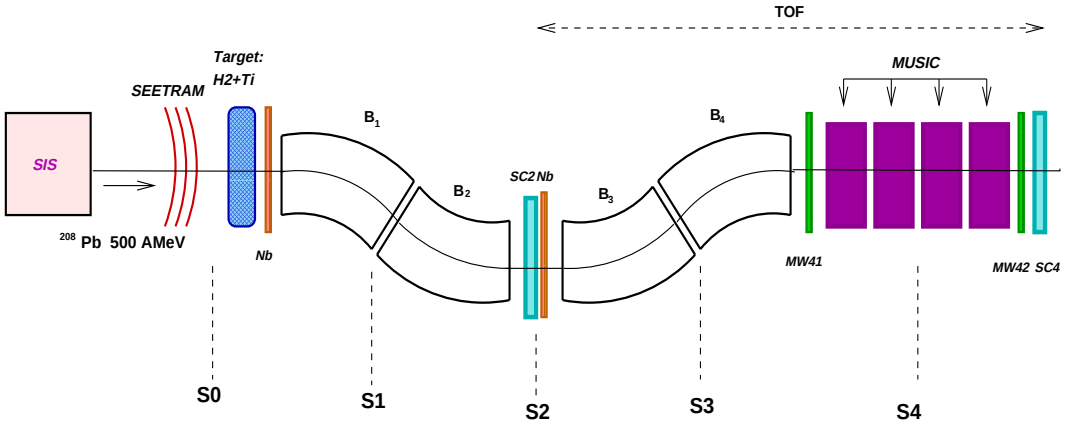

Figure 1. *Layout of the FRS experimental set-up for the experiment*

The lead beam was delivered by the heavy-ion synchrotron SIS at 500 A MeV. The beam intensity varied between 10^7 and 10^8 ions/spill, the spill length was

about 4 s with a typical repetition period of 8 s. The beam was controlled and monitored prior to the target by a Secondary Electron Transmission Monitor (SEETRAM) [30], which measured the number of incident particles. Then, the projectiles were focused onto a $(87.2 \pm 2.2)\ mg/cm^2$ thick liquid-hydrogen target [31] enclosed in a Ti container of $36.3\ mg/cm^2$ total thickness. Runs with a dummy target mocking an empty target were also done in order to subtract the contribution of the target walls. The produced fragments are focused in the forward direction due to the high incident energy. In order to maximize the number of bare ions passing through the FRS two niobium stripper foils of 60 mg/cm^2 and 221 mg/cm^2 thickness were placed behind the target and the 3 mm thick plastic scintillator placed at S2, (SC2), respectively.

2.2 Treatment of the experimental data.

The nuclei are identified with the help of the two plastic scintillators [32] (SC2, SC4) mounted at the intermediate S2 and final S4 focal planes, respectively, four ionization chambers (MUSIC), 40 cm long each and filled of P10 gas at twice the atmospheric pressure [33] and two multiwire proportional chambers (MW41, MW42) [34]. The presence of niobium stripper foils and of the four MUSIC's at high pressure was mainly intented for the detection of the fragmentation residues [27],

- From the Time-Of-Flight, TOF, between the scintillators at S2 (SC2) and at S4 (SC4) separated by 36 meters, one gets the fragment velocity, v:

$$v \propto 1/TOF \tag{1}$$

- The charge Z of the fragment is determined from the energy-loss ΔE information provided by the ionization chamber (MUSIC) through the relation:

$$Z^2 \propto \Delta E \times f(v) \tag{2}$$

  Since all the detected fission fragments have charges below Z < 60 and high kinetic energies, almost the totality of the ions is fully stripped. Therefore, the ionic charge is equal to the nuclear charge q=Z. The dependence on the velocity has been eliminated with the help of the preceding equation where $f(v)$ is an empirical function.
- The horizontal position measurements x_2, x_4 at the two focal planes S2 and S4 provide the magnetic rigidity of the nuclei in the second half of the spectrometer by the use of the ion-optical equations:

$$B\rho \propto g(x_2, x_4, V_4, D_4) \tag{3}$$

  where V_4 and D_4 are the magnification and the dispersion at the final focal plane, respectively.

The equation of the magnetic rigidity links these three measurements with the mass number by:

$$A \propto q\frac{B\rho}{\beta\gamma} \tag{4}$$

where q is the ionic charge, β the reduced velocity and γ the Lorentz factor.

Fig. 2 shows an example of the high resolution achieved in the identification pattern obtained from the energy loss and A/q information in a setting tuned for a magnetic-rigidity value of $B\rho$=9.17 Tm.

In order to cover the full range of the emitted fission fragments, two groups of settings were needed, one centered on nickel (Z=28) and the other on ruthenium (Z=44) isotopes.

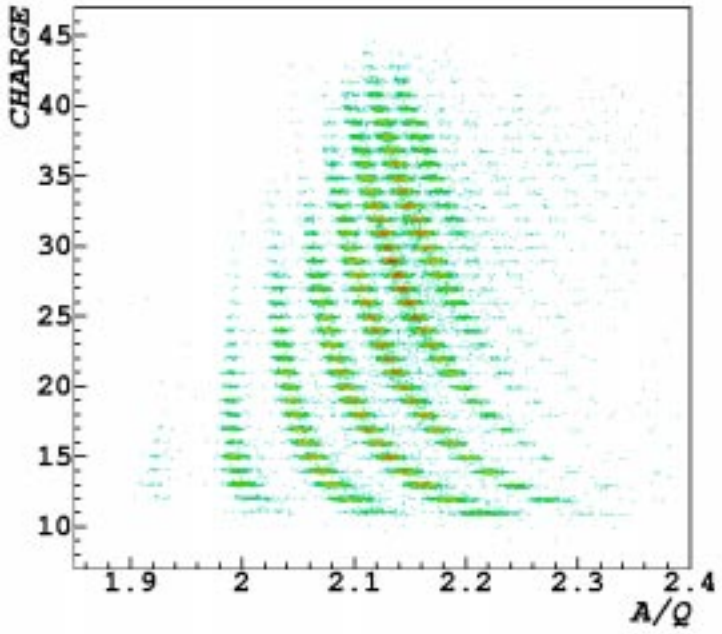

Figure 2. *Identification pattern: Charge values obtained from the energy loss in the MUSIC versus the A/q information given by the position and time-of-flight measurements for a setting centered at $B\rho$=9.17 Tm.*

2.3 Charge calibration.

The charge calibration is obtained from the projectile charge. However, since the fission-fragment charges are much smaller, this is quite delicate, and a particular care has been devoted to this calibration. Three settings centered

on different values of magnetic rigidity have been used. The first one is centered on $^{208}_{82}$Pb, the second one on $^{167}_{69}$Tm and the last one on $^{61}_{28}$Ni. From the superimposition of the energy-loss spectra we get the charge calibration by counting from the projectile charge value down to the fission region. Further, in order to optimize the range in energy loss to be able to detect the lightest fission fragments, the gain and the thresholds of the MUSIC detectors were changed. The same setting centered on ^{61}Ni was repeated under the two electronic conditions. Thus, due to the change of the electronics a new calibration had to be done. Both settings measured before and after the change of the electronics are represented in Fig. 3. The scales are not the same because of the different values of the gains, and also in Fig. 3 right) some lighter elements appear since the thresholds are lower.

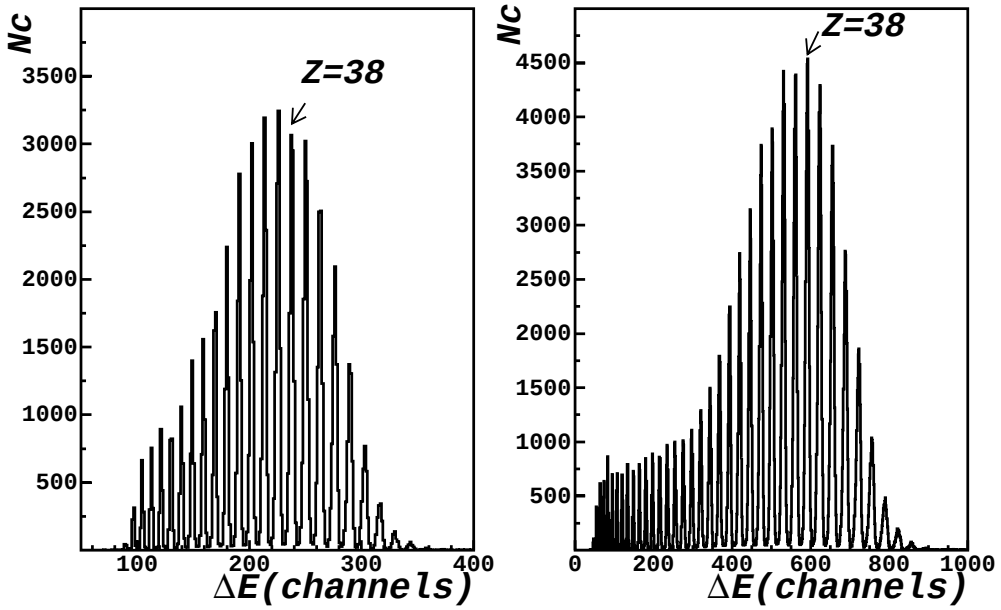

Figure 3. *Left: The energy-loss spectrum for a setting centered on ^{61}Ni before the change of the electronics. Right: The same spectrum after the change of the electronics (see text).*

First, a tentative Z-calibration is done by comparing the shapes of the distributions in the region of the heaviest fragments, the production of which is not expected to change. The peak labeled Z=38 in Fig. 3 left) has been determined by counting the peaks down from the beam with the low gain measurements. By comparing their normalized intensities and counting the peaks from the right side, the peak centered on channel 592 in ΔE in Fig. 3 right) can be attributed to the charge Z=38. However, to verify this hypothesis three independent methods have been employed:

- The method of the relative intensities.
  It is based on the fact that the relative production rate should be close to

1 when the reference peak chosen to normalize the spectra corresponds to the same Z value in both settings (see Fig. 4).

- The method of the position at S4.
  Since the deflection of the fragments in the magnetic fields of the spectrometer depends only on its magnetic rigidity value, the position at S4 of a given isotope in both settings, should be the same because the electronic of the position detectors has not changed.
- The method of the A/q values.
  This method has been already used for the identification of the lighter residues in the reaction ^{238}U on titanium at 1 A GeV [35]. The measurement of the energy loss in the MUSIC detectors is independent of the measurement of the A/q ratio, this one is obtained from the positions and from the TOF measurements (see equation 4). Therefore, with the A/q ratio one can get confirmation of the charge calibration by looking to the distances between two spots of the same charge on bidimensional plots like in Fig. 2.

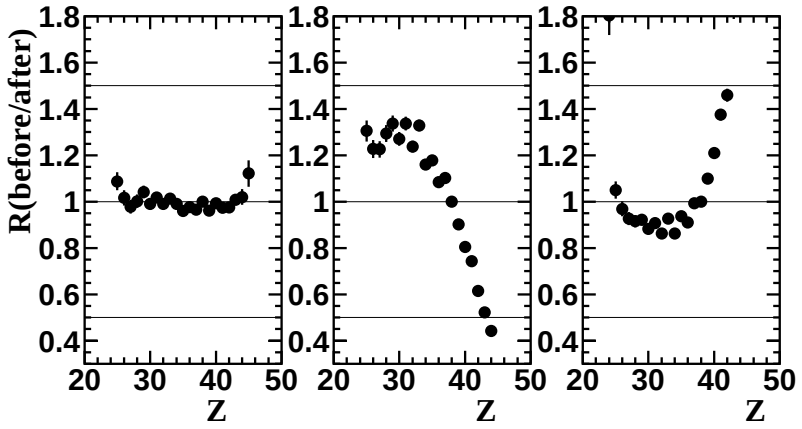

Figure 4. *Ratio of the relative Z peak intensities in the settings before and after the change of the electronics,* $R = [N_z/N_{38}]^{before}/[N_z/N_{38}]^{after}$. *Left: the relative intensities are normalized to the intensity of the peak labelled Z=38 in fig. 3 left (before) and right (after). Middle: The relative intensities after the change of the electronics have been normalized to the charge Z=39 in fig. 3 right (after). Right: The relative intensities after the change of the electronics have been normalized to the charge Z=37 in fig. 3 right (after). The error bars are associated to the statistical uncertainty.*

Fig. 4 illustrates the first method. For both settings, before and after the change of electronics, the relative intensity of each Z peak has been determined by normalizing them to the intensity of the peak supposed to be Z=38 in Fig. 3 (left and right respectively) and the ratio of the relative intensities for the two settings of electronics, $[N_z/N_{38}]^{before}/[N_z/N_{38}]^{after}$, has been plotted in Fig. 4 left). The ratio is constant and close to 1. On the contrary, if the peak labeled Z=38 in Fig. 3 right) (after the electronics change) is attributed to Z=37 or

Z=39, the values of the ratio are far away from 1 and no longer constant. This is shown in Fig. 4 (central and right panels respectively).

The two other methods described before, which are not illustrated here, corroborate this choice [36]. The convergence of the three independent methods leads to an unambiguous charge identification. The same procedure has been applied to the settings centered on the ruthenium isotopes.

2.4 Mass calibration

The absolute mass calibration has been carried out using the fact that a plot of the charge versus A/q should show a vertical line corresponding to A/q=2. However, it can be seen on Fig. 2 that the line A/q=2 deviates from a straight line for the lightest elements due to a Z-dependence of the TOF measurements. This could come from the fact that the stop detector at S4 was located behind the four MUSIC detectors. Consequently, supplementary criteria are needed in order to determine without any ambiguity the line corresponding to N=Z. A strong signature of the even-odd effect has been observed in the distribution of nuclides with N=Z produced in the reaction ^{56}Fe+p at 1 *A* GeV [37] as well as in the production of the lighter elements in the spallation reaction of uranium on titanium [35]. Therefore, we have looked at the mass distribution of nuclei associated with the line A/q=2 previously determined and compared to what would result if we assume N=Z-1 or N=Z+1. The mass distributions for the different assumptions are represented in Fig. 5.

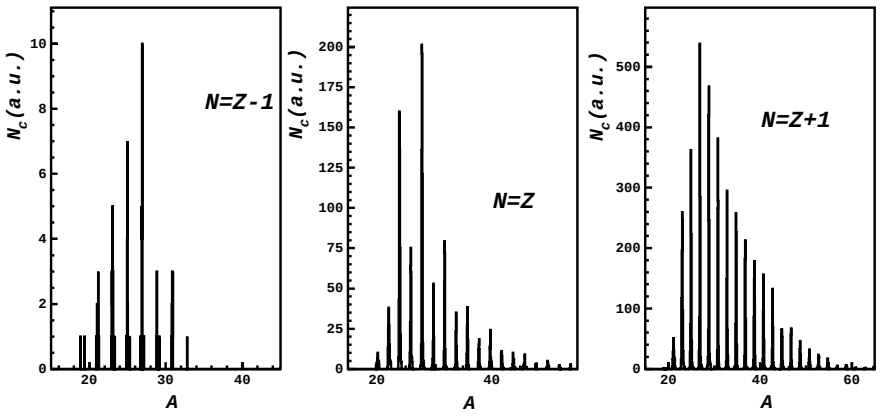

Figure 5. *Mass distributions for three lines of constant A/q in the identification plot of Fig. 2. One for lower A/q values than the assumed A/q = 2 line (left), another on that line (center) and the last one for higher A/q values (right).*

Only the central panel in Fig. 5 is presenting the even-odd signature. For the other panels in Fig. 5 the effect disappears. This effect allows to confirm

the mass calibration. For heavier fission fragments measured with the setting centered on Ru, the mass of the projectile has been used for mass calibration.

2.5 Normalization

The SEcondary Electron Monitor (SEETRAM [30]) was used to monitor the beam intensity. The detector is formed by three aluminum foils of total thickness 8.9 mg/cm^2. The external foils at positive potential (+80V), collect the secondary electrons created by the passage of ions. The central grounded foil is hence positively charged and gives a current proportional to the number of incident ions. In order to set a relation between the number of secondary electrons and the number of the incident ions, a scintillator which measures directly the number of ions in the beam was placed after the SEETRAM during the calibration runs at lower intensities avoiding saturation of the scintillator. An example of the beam structure as a function of the time is presented in the Fig. 6.

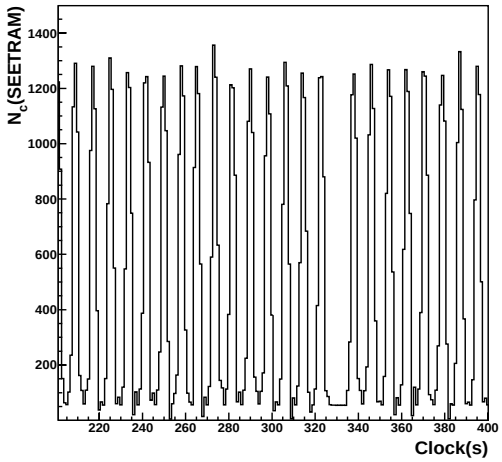

Figure 6. *Spectrum of the numbers of counts in the SEETRAM as a function of time.*

The background seen in Fig. 6, in between two contiguous spills of the beam, is due to the electronic-offset current. This background has to be subtracted to obtain the real number of counts in the SEETRAM. In order to avoid saturation effects in the scintillator, the rate was kept lower than 10^5 particles/s. The calibration was done increasing the beam intensity from 10^2 up to 10^6 particles/s.

The mean number of particles detected in the scintillator per spill is plotted in Fig. 7 as a function of the corresponding number of counts measured by the SEETRAM.

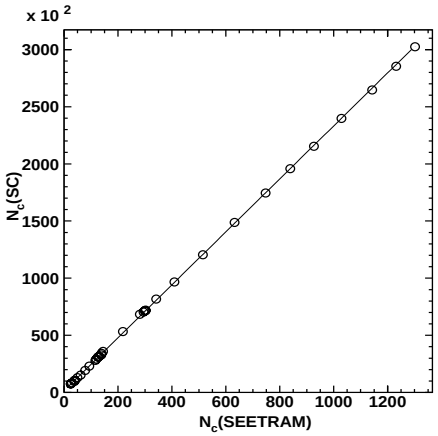

Figure 7. *Linear fit between the number of the particles detected by the scintillator and the number of counts measured with the SEETRAM. Errors are smaller than the symbol size.*

This figure shows a linear dependence until $\sim 10^5$ particles/s, above this limit the calibration is no longer linear. The present calibration factor is $F_{SEE} = 231 \pm 7$ numbers of ions per count in the SEETRAM obtained for a sensitivity of $\epsilon = 10^{-8}$, giving a current of $10^{-8}A$ for an output signal of 1 V. This value is in agreement with the one reported in ref. [30]. The uncertainty in the calibration factor was calculated from the different results of the calibration factor obtained using either a linear fit or a second degree polynomial, taking the coefficient of the linear term. The total uncertainty is less than 4%.

2.6 Reconstruction of the velocity distribution and window subtraction

In these experiments, not only full identification has been obtained but also the kinematic properties of the fragments have been measured. Once the identification was done in the second stage of the spectrometer, the velocity can be obtained from the magnetic rigidity in the first stage of the spectrometer by the following equation:

$$\beta\gamma \propto \frac{(B\rho)_1}{A/q} \qquad where \qquad (B\rho)_1 = B\rho_0 \left(1 + \frac{x_2}{D_2}\right) \tag{5}$$

where A is the atomic mass number, $(B\rho)_1$ is the magnetic rigidity in the first stage of the spectrometer, $(B\rho)_0$ is the magnetic rigidity of the central trajectory and D_2 the dispersion at the intermediate focal plane.

Corrections have been done in order to compensate the velocity changes due to the energy losses in the layers between the interaction point and the first

dipole. In addition, the slowing down of the projectile in the target before interacting has been taken into account by applying the average energy loss of half the target. Finally, the Lorentz transformation has been applied to get the velocities in the rest frame of the lead ion beam.

2.6.1 Effect of the momentum acceptance of the spectrometer

Because of the limited acceptance of the FRS spectrometer, only a part of the momentum distribution for a given isotope is transmitted in one setting of the FRS magnets. The velocity distribution of the fission fragments is given by the physics of the nuclear reaction. The two partners involved in a fission event are emitted back to back with an angle of 180 degrees. Therefore, in the center-of-mass system the momentum space of the fission fragments occupies a hollow sphere with a radius corresponding to the Coulomb repulsion. This sphere becomes an ellipsoid in the laboratory frame due to the Lorentz transformation. The spread of measured fragment velocities can be obtained from the difference between the forward and backward emitted fragments in the laboratory system. At 500 A MeV incident energy, for a fission fragment, it can vary from $\Delta p/p = 8\%$, for Z=50, A=117, up to $\Delta p/p = 15\%$, for Z=23, A=63. Since the momentum acceptance of the FRS is about $\Delta p/p = \pm 1.5\%$ several magnetic settings are needed to cover the complete velocity distribution, as it is shown in the Fig. 8 left).Therefore, the full momentum distribution can only be measured by scanning different $B\rho$ values and summing the different measurements with the correct normalization.

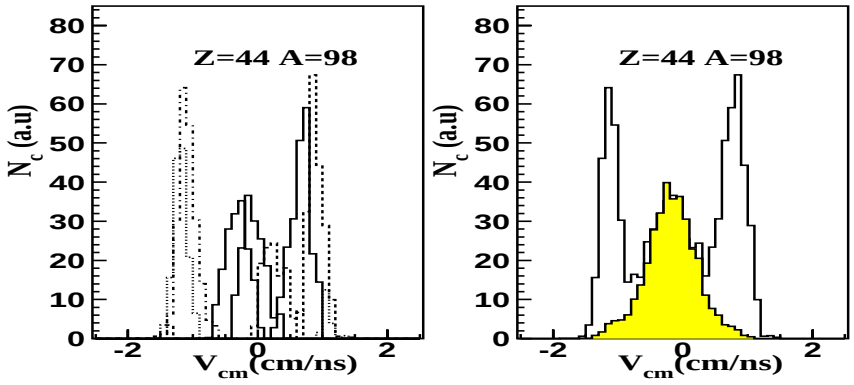

Figure 8. *Left: Superimposition of the different single velocity spectra corresponding to the isotope Z=44, A=98 measured with each setting. Right: The complete velocity distribution for the isotope Z=44, A=98 on the filled target, open histogram, superimposed to the one obtained with the dummy target, grey histogram.*

The final shape shown in Fig. 8 right) has been obtained from the maximum yield for each velocity value in Fig. 8 left). A more general and graphical

description can be found in references [4, 7, 35, 38].

2.6.2 Window contribution

The contribution coming from the reactions with the walls of the target, including the production from the SEETRAM and of the thin titanium vacuum window behind SIS, has been subtracted directly from the velocity spectra. For the fission fragments this contribution varies between 2-3% for the neutron-rich nuclei and it follows an exponential trend when decreasing the mass number reaching values around 20-30% for neutron-deficient nuclei, as shown in Fig. 9.

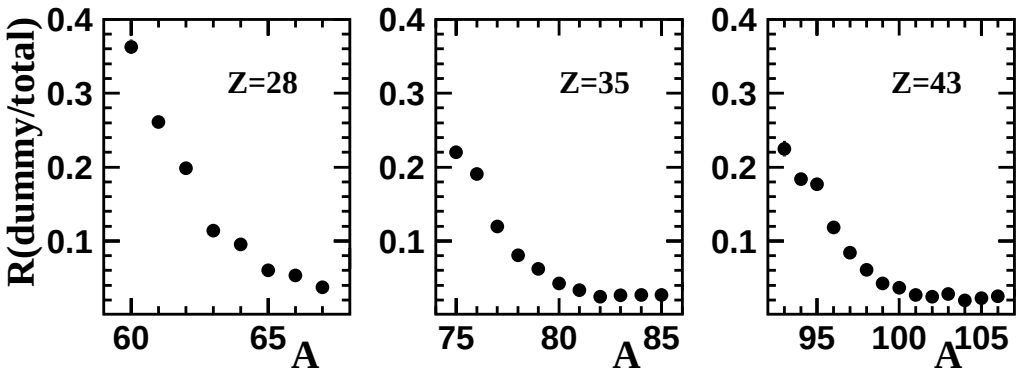

Figure 9. *Ratio between the contribution due to the dummy target and the one of the total target as a function of the mass, for three elements of Z=28, 35, 43.*

However, the contribution of the dummy target is small on the whole, thanks to the relation of the total reaction cross-sections and of the number of atoms between the titanium and the hydrogen targets.

2.7 Determination of the isotopic cross-sections and the correction factors

The cross-section for each fission fragment has been obtained from the measured counting rate, $Y(Z, A)$ normalized to the number of incident particles, N_{pro}, and to the number of atoms per area in the target, N_{at}. In order to remove the contribution of the walls of the target the same measurements have been repeated with a dummy target mocking an empty target cell. With appropriate normalization, this contribution has been subtracted to obtain $Y(Z, A)$. In

addition, correction factors leading to losses or gain in the number of detected ions have to be taken into account. Therefore, the final cross-sections are given by:

$$\sigma(Z,A) = \frac{Y(Z,A)}{N_{pro}N_{at}} f_\tau f_\epsilon f_{tr} f_{tar} f_{sec} f_q \tag{6}$$

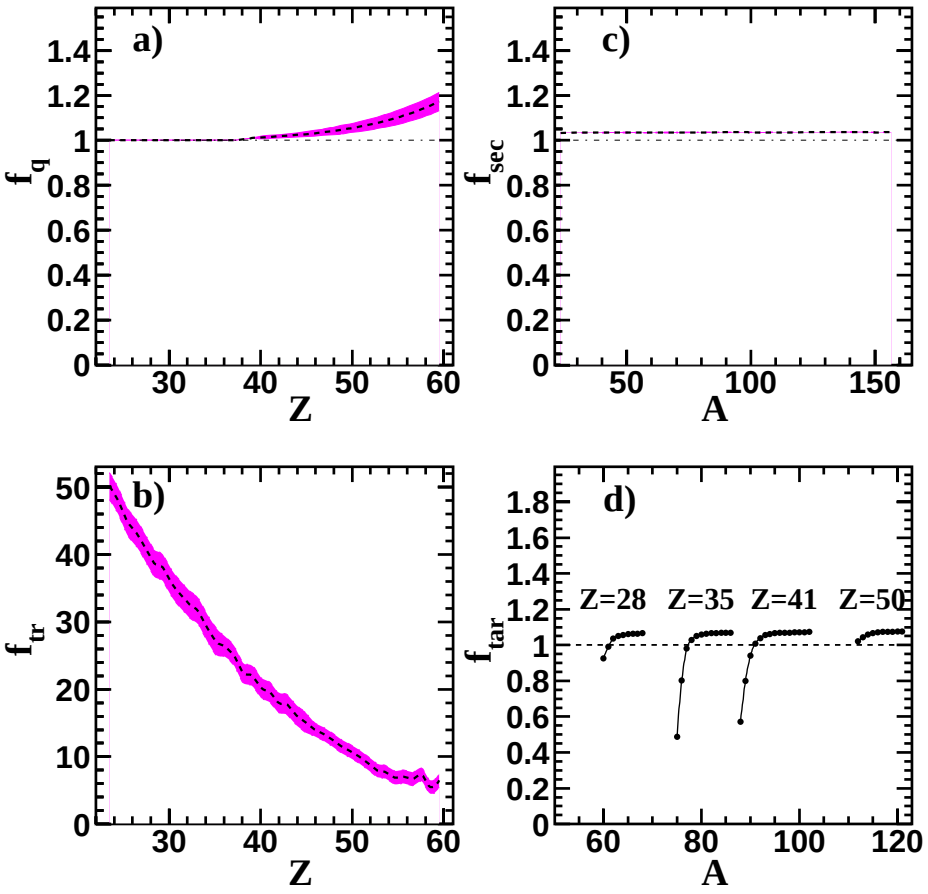

Figure 10. *a) Correction factor due to the incompletely stripped ions f_q. b) Correction factor accounting for the angular acceptance of the spectrometer f_{tr}, for the backward component. c) Correction factor for secondary reactions f_{sec} in the layers located in the beam line d) Correction factor for secondary reactions f_{tar} inside the liquid-hydrogen target for four elements: 28, 35, 41 and 50.*

The correction factors are :

- f_τ that corrects for the dead time of the data-acquisition system.
- f_ϵ which takes into account the inefficiency of the detectors.

- f_{tr} that corrects for the part of the isotope angular distribution not transmitted in the spectrometer because of its angular acceptance.
- f_{tar} and f_{sec} which account for the losses or gains due to secondary reactions in the target and in the scintillator placed at S2, respectively.
- f_q that corrects for the loss of non-fully stripped ions.

The correction factors f are defined by $r = f \times m$, where m is the measured number of a given product and r is the real produced number. The most important ones are presented in the Fig. 10 with the associated uncertainties.

2.8 Charge states

In our procedure only fully stripped ions in the magnetic sections before S2 and between S2 and S4 are analysed. In the upper part of Fig. 10 a) f_q, the correction factor accounting for the existence of non-fully stripped ions is shown as a function of the nuclear charge. f_q is always close to 1 except for the heaviest fission fragments for which it reaches 1.16. The rate of fully stripped ions was calculated by using the GLOBAL code [39]. The systematic uncertainty associated to the factor, which has been represented on Fig. 10 a) by the grey area, was estimated by comparing the results of two codes describing the interaction of ions with matter: GLOBAL and AMADEUS [40]. The uncertainty on f_q varies from 4% to 1% for the charges Z=60 and Z=40, respectively.

2.9 Transmission correction factor

The angular acceptance of the spectrometer cuts the angular distribution of the fission fragments. The maximal angle of emission in the laboratory frame for each fission fragment, θ_{max}, can be obtained from the expression:

$$\theta_{max} \propto \frac{\beta}{\gamma_0 \beta_0} \tag{7}$$

where β and β_0 are the reduced velocities of the fission fragment in the frame of the fissioning nucleus and the projectile in the laboratory frame respectively, γ_0 is the projectile Lorentz factor. This angle ranges from $\theta_{max} = \pm 48$ mrad, for Z=28, A=63, down to $\theta_{max} = \pm 25$ mrad, for Z=50, A=110, while the angular acceptance is $\theta_{acc} \sim \pm 15$ mrad.
This implies that the fragments emitted perpendicularly to the beam axis are cut by the angular acceptance of the spectrometer. Therefore, only forward

and backward emitted fragments could be detected. This is the reason why the projection of the velocity distribution on the axis parallel to the beam velocity in Fig. 8 right) shows two peaks centered around $v_{cm} = \pm 1.0\ cm/ns$. The central peak close to $v_{cm} = 0.0\ cm/ns$ in Fig. 8 comes from another reaction mechanism, namely fragmentation in which only one heavy fragment is produced. The number of ions transmitted with respect to the produced ones defines the transmission of the spectrometer. Although this property restricts the transmission, it turns out to be a kinematical way to separate both mechanisms, fission and fragmentation present in the spallation reaction. Actually, the fragmentation peak is only due to the target container as shown in Fig. 8 right), this mechanism on hydrogen does not populate the low-Z elements [27].

In Fig. 10 b) the transmission correction factor, f_{tr} for the backward component, is represented versus the charge of the fission products. The transmission correction factor decreases when the charge of the detected fragments increases. Because light fission fragments have the highest velocities, they are more affected by the cut of the angular acceptance. In this experiment, the transmission of the fission fragments through the spectrometer was rather small because of the low beam energy, 500 A MeV. It is important to note that for some lightest fragments only 4% of the total production is detected. This points out the limit of this experimental method for energies lower than 500 A MeV. To determine the correction factor f_{tr} we used the procedure described in the reference [38]. In this calculation, a map of the angular acceptance $\alpha_{acc}(x_2, x_4)$ of the spectrometer obtained from a complete ion-optics simulation, was computed as a function of the positions of the fragments at the second and at the final focal plane. The correction factor is given by the following expression:

$$T = \int_0^{\alpha_{acc}(x_2,x_4)} \left(\frac{dI}{d\Omega}\right) d\Omega \tag{8}$$

where $\left(\frac{dI}{d\Omega}\right)$ is the residue angular distribution, supposed to be isotropic in the fissioning system frame, and is integrated within the limits given by the angular acceptance $\alpha_{acc}(x_2, x_4)$ of the spectrometer after having been transformed into the laboratory system. The uncertainty on f_{tr} consists in two parts: one error estimated at 5%, due to the geometrical constraints of the FRS, the other one due to the uncertainties on the fragment velocity which is between 5% for the light charges and 7% for the heaviest ones. The global uncertainty on f_{tr} ranges between 11% and 13%.

2.10 Secondary-reaction correction factor

Due to secondary reactions, the measured number m of a given product is the real primary number r modified by gained or lost number gl of this product, $r = m \pm gl$. The correction factors f are defined by $r = f \times m$ then

$$f = 1 \pm (gl/m) \tag{9}$$

the quantity $g = gl/m$ is obtained through the needed reaction cross-sections.

2.10.1 Secondary reactions at S2.

The correction factor f_{sec} associated to the loss of part of the fragments due to the secondary reactions in the layers of matter placed at S2 was given by the interaction probability in the different materials. The cross-sections of nuclear interactions have been calculated using the Karol formula [41]. The loss due to secondary reactions increases slightly with the mass number with a maximum value of f_{sec} of about 1.07 for the heaviest masses (see Fig. 10 c). The uncertainty on g associated to the reaction cross-sections is 5%. This leads to a maximum error of 0.35% on f_{sec} and hence can be disregarded.

2.10.2 Secondary reactions in the target

The measured isotopic distribution can also be distorted by secondary reactions in the liquid-hydrogen target. Thus, it is very important to estimate the contribution coming directly from the primary production. Secondary reactions in the liquid-hydrogen target have been calculated with the help of the formalism developed in the reference [42]. Two mechanisms can contribute to the production of a given fission fragment (Z, A): The fission of a primary evaporation residue (fragmentation-fission) and the fragmentation of a fission fragment (fission-fragmentation). In the first case, the primary evaporation residues still have a high fissility and have a second chance to fission. The probability to produce a fragment by this way has been estimated to be lower than 3% because the number of produced fragments with a high fission probability is rather small. However, the second mechanism, fission-fragmentation, is more important and leads to a depopulation of the heaviest fragments ($f_{tar} > 1$) in favor of the lightest ones ($f_{tar} < 1$). In order to simulate the production by fragmentation of fission products the INCL4/ABLA code was used. This choice is justified because the code has been shown to reproduce quite well the total reaction probabilities and the isotopic distributions of fragmentation products close to the projectile for different systems [20].

In Fig. 10 d) it is shown that this correction depends on the isotope masses. For a given element, neutron-rich isotopes are lost through secondary reactions so their yields should be multiplied by factors around 1.10 while neutron-deficient isotopes are gained leading to correction factors that can reach around 0.4. This is due to the fact that the fragmentation tends to produce nuclei with N/Z ratio smaller than the primary fragment. The uncertainty on g of the number of gained or lost isotopes was estimated to be 10%, that means 1% on the correction factor f_{tar} for most of the fragments.

2.11 Uncertainties

The relative uncertainty on the isotopic cross-sections has been divided into a statistical and a systematical one due to the calibration and corrections procedures. Both are given in the tables of the appendix. The statistical uncertainty includes the one coming from the subtraction of reactions in the dummy target. It is always lower than 5-7%. For a given charge, the statistical uncertainty increases for the neutron-deficient isotopes since the contribution of the empty target is more important, and also for the neutron-rich side because the number of detected events decreases.

The systematical uncertainty ε can be expressed as follows:

$$\begin{aligned}\varepsilon^2(\sigma) = \varepsilon^2(sep) + \varepsilon^2(N_{at}) + \varepsilon^2(F_{SEE}) + \varepsilon^2(f_{tr}) \\ +\varepsilon^2(f_q) + \varepsilon^2(f_{sec}) + \varepsilon^2(f_{tar})\end{aligned} \tag{10}$$

where $\varepsilon(sep)$ is the uncertainty due to the separation method between two adjacent isotopes (see Fig. 2) and it amounts to less than 1%, $\varepsilon(N_{at})$ is the uncertainty in the measurement of the target thickness, $\varepsilon(F_{SEE})$ comes from the SEETRAM calibration, and $\varepsilon(f_{tr}), \varepsilon(f_q), \varepsilon(f_{sec}), \varepsilon(f_{tar})$ are the uncertainties associated to the correction factors discussed in the previous sections. A summary of the most important systematical uncertainties is presented in the table 1.

Actually, the systematical uncertainty is slightly dependent on the considered isotope. It varies from 13% to 20 % for the isotopes Z=25-50, the most important values being for the isotopes placed at the end of the isotopic distributions. Below Z=25 and above Z=50, the total (statistical plus systematical) uncertainty can reach 35-45 %. Only isotopes with total relative uncertainties smaller than 50% have been reported in the table given in appendix. One must notice that the present discussion on uncertainties concerns the absolute values. The errors on the relative values are much smaller, of the order of a few percents, except for a few isotopes on the very end of the distributions.

	uncertainty (%)
target thickness	$\varepsilon(N_{at})$=2.5
SEETRAM calibration	$\varepsilon(F_{SEE})$=4
transmission	$\varepsilon(f_{tr})$=13
charge states	$\varepsilon(f_q)$= 4
secondary reactions in the target	$\varepsilon(f_{tar})$=1
Total mean uncertainty	ε_{tot}=14

Table 1
Mean systematical relative uncertainties expressed in % for each correction factor applied to the calculation of the cross-sections.

3 Experimental Results

3.1 Isotopic distributions

The measured isotopic distributions are presented in Fig. 11. Only statistical uncertainties are reported. The complete data are tabulated in the appendix. It can be seen that all fragments with cross-sections down to 0.1 mb have been measured. The position of the maximum of the isotopic distribution evolves from the neutron-rich side not far away from the stability line (marked by arrows), for the lightest elements, to the neutron-deficient side, for the heaviest ones. This N/Z variation will be discussed in section 3.6 more thoroughly.

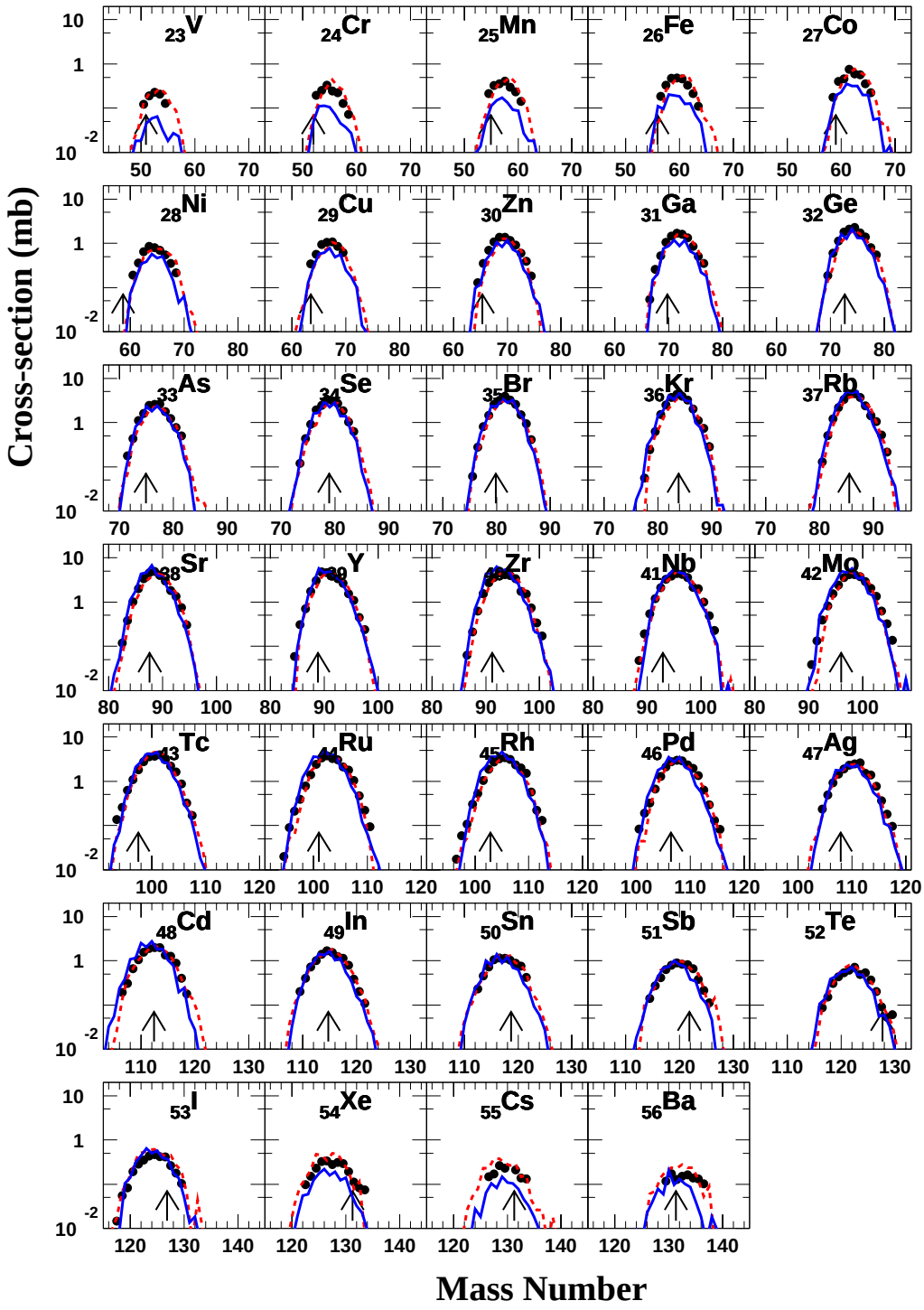

Figure 11. *Isotopic cross-sections. Only statistical error bars are shown. The arrows indicate the valley of stability. The lines are theoretical calculations (discussed in section 5) with INCL4+ABLA (dashed lines) and the INCL4+GEM codes (solid lines) renormalised to the experimental total fission cross-section.*

In this section, we report on the comparison between our data and the ones obtained by the group of R. Michel from Hannover University [15, 16] by using the γ-spectrometry method. In this experiment, a stack of natural lead and aluminium foils was irradiated by protons at different energies and in particular at 553 MeV. The residual radionuclides were identified by off-line γ-spectrometry. Independent and cumulative cross-sections were measured. In order to compare our data to the cumulative cross-sections, it was necessary to sum our results along all the decay branches (generally beta decay) by using the expression given in the reference [16].

In Fig. 12, we show the comparison between the FRS and the γ-spectrometry data at 500 A MeV. The upper panel shows the cross sections and the bottom one, the ratio between the FRS and γ-spectrometry measurements.

The present data are generally a little bit higher than the ones measured using the γ-spectrometry method. Nevertheless, the agreement is rather good. Among the 27 points compared, 18 of them are within the error bars. However, some isotopes show significant differences. The ^{54}Mn presents a deviation factor 2.2 but still in agreement with our result because of the large uncertainty given by Gloris et al., the ^{65}Zn a factor 1.6, and the ^{101}Rh is about a factor 4 higher. For the two first isotopes, the disagreement is unclear since the decay schemes seem to be well determined. The isotope ^{101}Rh was cited in the reference [16] as a cumulative isotope with an isomeric transition rate of 92.3%. However, this value corresponds to the yield of the electronic capture transition. This mistake could explain an underestimation because the isomeric state decays more preferentially by electron capture than to the ^{101}Rh ground-state.

Apart from a few examples, the observed differences could be due to a global factor. The average value of the ratio is 1.11 ± 0.04. However, it has to be noticed that the γ-spectrometry measurements have been done with a natural lead target at 553 MeV. The difference in the energy should not lead to significant differences if one refers to Prokofiev's systematics [43]. The average fissility of the natural lead is expected to be higher than the one of the isotope 208 since the average mass is 207.2. This difference should be taken into account in the comparison of the cross-sections. According to [43], the ratio of the total fission cross-section induced by protons between natural lead and the isotope 208 has been estimated to be 1.1. Therefore, the value of the ratio should be increased by this value in the average. Consequently, the ratio between the present and Gloris et al. cross-sections at 500 A MeV can be estimated to be:

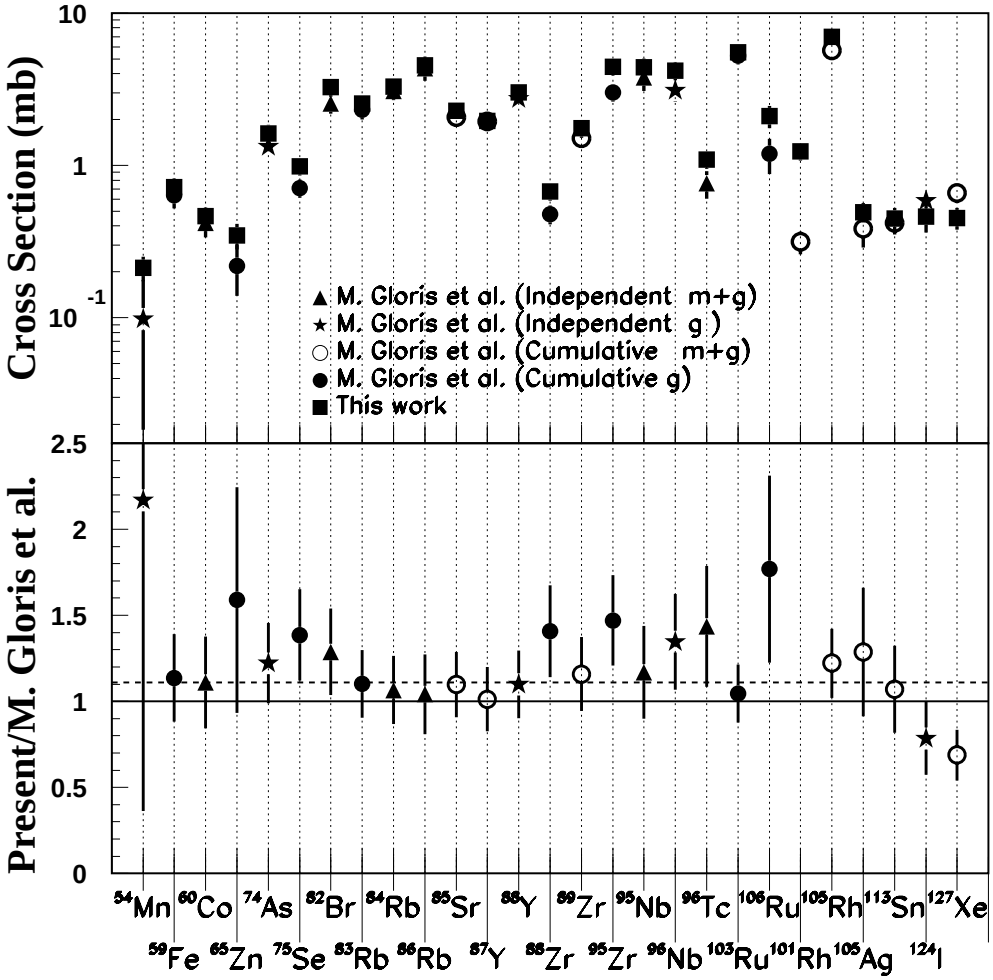

Figure 12. *Upper panel: Experimental cross-sections from GSI (^{208}Pb) and from R. Michel (^{nat}Pb) et al. [15, 16]. The meaning of the various symbols is given in the figure. Independent and cumulative yields as well as measurements of metastable (m) and ground (g) states are also indicated [15, 16]. Bottom panel: Ratio of the cross-sections. The uncertainties represented are the systematic and the statistical ones. The dashed line is the average value (1.11) of the ratio.*

$$R_{present/Gloris} = 1.22 \pm 0.04$$

still compatible within the systematics uncertainties ($\sim 15\%$) of both experiments .

In order to see if this behaviour could be due to a more general trend related to the difference of experimental techniques, we have carried out a comparison of 1000 A MeV data from Gloris et al. in the same paper with the data obtained previously by our collaboration at GSI [4]. The results of the ratio of cross-sections (FRS/γ-spectrometry) are shown in Fig. 13 as a function of the mass of the residues, for fission and evaporation residues. The present data at 500 A MeV are also displayed.

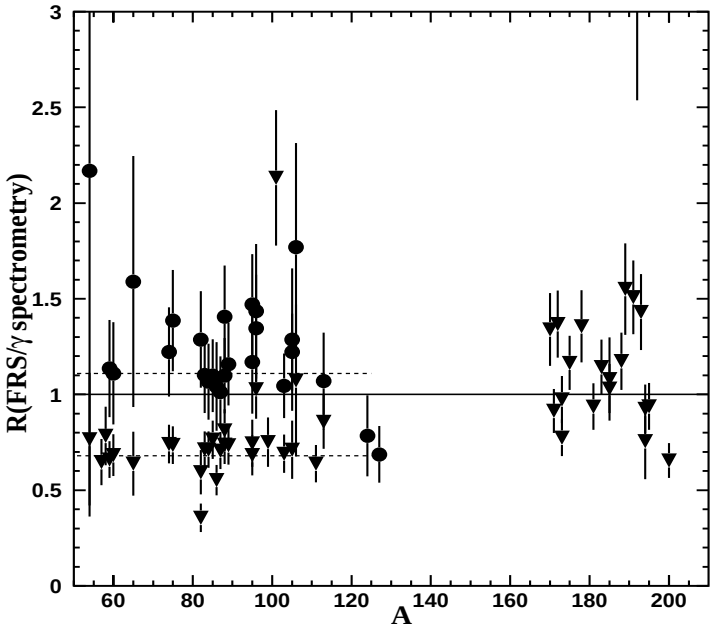

Figure 13. *Ratio of the cross sections between GSI and γ-spectrometry data. The uncertainties represented are the systematic and the statistical ones. Full points are for the present fission data at 500 A MeV, inverted triangles are for 1000 A MeV fission and residue measurements [4]. The dashed lines are the average values of the ratio for each set of data.*

In the region of masses $A > 160$ corresponding to the evaporation residues at 1000 A MeV, the ratio between the cross-sections is statistically distributed around 1. This could be an indication that there is no global normalisation factor discrepancy between the two methods. However, in the fission region, with $A < 134$, the FRS data at 1000 A MeV are systematically below the γ-spectrometry ones. In fact, the average value of the ratio at 1000 A MeV is 0.68 ± 0.02 in the fission region. Taking into account the difference between ^{208}Pb and natural lead, the mean ratio is increased by 10% and becomes:

$$R_{GSI/Gloris} = 0.75 \pm 0.02$$

This discrepancy is a little larger than at 500 A MeV but surprisingly it is now in the opposite direction.

Another measurement by γ-spectrometry on ^{208}Pb at 1 GeV has been recently reported by Titarenko et al. in [44]. If we compare their results to the FRS ones at 1 GeV [4], for the fission isotopes measured in both experiments and after cumulation of the FRS cross-sections, we find that ref. [44] cross-sections are 31% higher on the average. The same group has very recently measured excitation functions for the same system [45]. Only partial results are presented in the paper, but the dependence with energy of the few comparable fission isotope cross-sections (^{59}Fe and ^{86}Rb) seems to be in contradiction with the one we have found between 500 and 1000 MeV.

No clear explanation for the discrepancies discussed in this section has been found. We will come back to this problem in section 3.5.

3.4 Charge and mass distributions

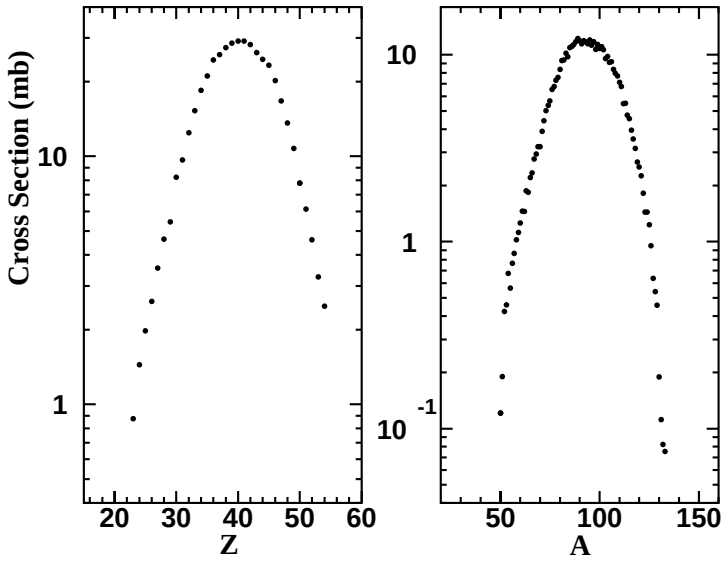

Figure 14. *Charge (left) and mass (right) distributions of the fission fragments.*

The charge and mass distributions of the fission fragments are shown in Fig.

14. They are nearly symmetric and their respective mean values are

$$< A >= 93.0 \pm 0.4 \text{ and } < Z >= 40.0 \pm 0.1,$$

with widths (obtained from a gaussian fit) equal to

$$\sigma_A = 15.1 \pm 0.6 \text{ and } \sigma_Z = 6.3 \pm 0.2.$$

We can compare our results to those obtained at different energies on similar systems. This is done in table 2 where the mean values and widths of the charge and mass distributions are given. Our results are in excellent agreement with the values reported by E. Hagebø and T. Lund [46], which have measured the yield of a few isotopes produced in the fission of natural lead with protons at 600 MeV.

Reaction	A	Z	σ_A	σ_Z
$^{208}Pb + p$ (500AMeV)	93.0 ± 0.4	40.0 ± 0.1	15.1 ± 0.6	6.3 ± 0.2
$^{nat}Pb + p$ (600AMeV)	93.2	40.0 ± 0.1	14.9 ± 0.1	6.34 ± 0.1
$^{208}Pb + p$ (1000AMeV)	90.7 ± 1.0	39.6 ± 0.5	16.1 ± 0.8	6.6 ± 0.3
$^{208}Pb + d$ (1000AMeV)	89.6 ± 1.1	39.0 ± 0.7	17.4 ± 1.0	7.3 ± 0.5

Table 2

Mean values and widths of the charge and mass distributions of fission fragments in the reactions $^{208}Pb + p$ (500 A MeV, this work), $^{nat}Pb + p$ (600 A MeV) [46] and $^{208}Pb + p$ (1000 A MeV),$^{208}Pb + d$ (1000 A MeV) [4].

In order to complete the study of the energy dependence, the system $^{208}Pb+d$ (1000 A MeV) [5] has been considered to be almost equivalent to the $^{208}Pb+p$ (2000 A MeV) system. This can be justified by the observation of Ledoux et al. [48] that at the same total incident energy the number of evaporated neutrons is independent of the type of the incident particle inducing the reaction. Therefore, the excitation energy deposited in the nucleus can be supposed depending only on the total incident energy.

The mean values of the mass and charge distributions decrease with increasing incident energy. This can be explained in terms of the excitation energy at the end of the intranuclear cascade. Indeed, the higher the projectile energy, the higher is the energy deposited in the prefragment. If the excitation energy of the prefragment is higher, then the evaporation of protons and neutrons increases leading to lighter fissioning nuclei. Furthermore, the excitation energy left to the fission fragments is also higher leading to even lighter fission fragments. On the contrary, the widths follow the inverse behavior. The widths of the charge and mass distributions get wider with increasing incident energy:

this is simply due to to the broader excitation energy distribution at higher beam energy and to the fact that more statistical evaporation induces more fluctuations on the final distributions.

3.5 Total fission cross-section

Adding the individual isotopic cross-sections obtained in the reaction $^{208}Pb{+}p$ at 500 A MeV for the elements from vanadium up to barium and dividing by two to take into account the binary nature of the process, the total fission cross-section is

$$\sigma_f = 232 \pm 33 \text{ mb.}$$

The uncertainty corresponds to the systematical one discussed in section 2.11. This value can be compared to previous evaluations or measurements for lead at similar energies, as shown on the first column of table 3. Our value is 55% higher than the one obtained by E. Hagebø and T. Lund [46] $\sigma_f = 149 \pm 6$ mb from the integration of the mass distribution in the reaction $^{nat}Pb + p$ at 600 MeV. A systematics obtained from the evaluation of different experiments on ^{208}Pb and ^{nat}Pb at different energies has recently been proposed by Prokofiev [43]. According to it, the total fission cross-section induced by protons at 500 A MeV of ^{208}Pb is 118 mb. This value is about a factor 2 lower than the one measured here. Note that in the systematics of reference [43], there are no experimental points for the total fission cross-sections of ^{208}Pb between 100 A MeV and 1000 A MeV bombarding energies, while for ^{nat}Pb there is only the one from Hagebø et al. [46], the uncertainty associated to this measurement was estimated to be 20% in [43]. From the comparison between Gloris et al. [16] and our data, done in section 3.2, it was concluded that their cross-sections were 1.22 smaller than ours. This can be used to roughly estimate a total fission cross-section value for data from [16], which is given in table 3. A 20% error has been arbitrarily given to our evaluation. The same can be done for their 1 GeV results [15] with our ratio of 0.75. A comparison of the cross-sections at this energy is shown in the second column of table 3. Fig. 15 shows the overview of the known data as a function of incident energy including the Prokofiev's systematic (solid line).

According to Fig. 15 and table 3, it is clear that the measured total fission cross-sections present a large dispersion. In fact, the data obtained by Hagebø et al. [46] at 600 MeV, Vaishnene et al. [47] at 1000 MeV and Enqvist et al. [4] at GSI (1000 A MeV) are in agreement with the Prokofiev's systematic (which has been done taking into account the first two sets of data) within the error bars. On the other hand, the experimental values obtained in this

	$E_{inc}(MeV) \simeq 500$	$E_{inc}(MeV) \simeq 1000$
GSI (this work, [4])	232 ± 33	163 ± 26
Estimated using ([15],[16])	190 ± 40	220 ± 45
E. Hagebø et al. [46]	149 ± 30	
A. V. Prokofiev ([43])	116	116
L. Vaishnene et al. ([47])		132 ± 13, 142 ± 14

Table 3
Known experimental total fission cross-sections in mb for Pb+p reactions. Cross-sections from R. Michel et al. data have been estimated in the present work.

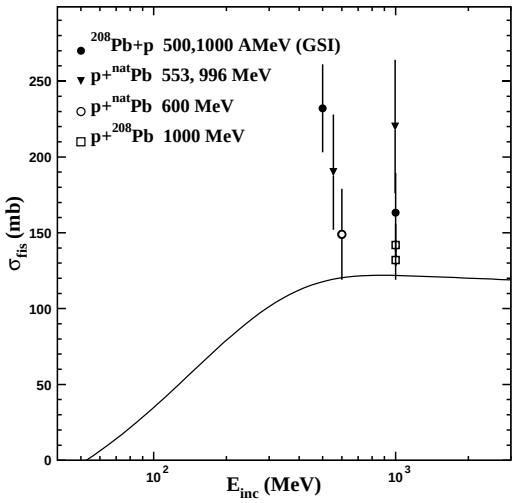

Figure 15. *Total fission cross-section as a function of incident energies: Symbols are experimental data given in table 3 and the full line corresponds to the Prokofiev's systematic for the ^{208}Pb.*

work and those estimated from [16] and [15], are substancially higher.

Furthermore, the total reaction cross-section

$$\sigma_{reac} = 1670 \ \pm \ 71 \text{ mb}$$

obtained from the sum of our fission cross-section plus the evaporation residue cross-section (1438±38 mb) measured during the same experiment [27], is in good agreement with what is expected from the systematics of [49], i.e 1700 mb.

It is also very surprising that the total fission cross-sections measured by the same inverse-kinematics methods are found to decrease with incident in-

creasing energy, contrary to what is obtained from Prokofiev's systematics (a constant behaviour) or from the extrapolation of Michel's group data (a slight increase).

No explanation for these discrepancies have been found. In the experimental procedure used in FRS experiments, a possible source of error that could have been underestimated is the transmission correction factor. We have suspected for a while the validity of the assumption that the emission of the fission fragments was isotropic in the center-of-mass, which, as said in section 2.11, was used to determine the transmission correction factor. We have made a carefull simulation of this effect with the INCL4/ABLA code, which provides the angular momentum at the end of the INC stage, deducing the corresponding anisotropies from [50, 51]. Although the resulting anisotropy is non negligible in the system of the fissioning nucleus, the effect is completely washed out because the directions of the recoil velocity and of the angular momentum of the nucleus after the INC stage fluctuate very much. The result is that the effect on the transmission factor is always smaller than a few percents, justifying a posteriori our assumption.

In view of the preceeding discussion it is clear that dedicated measurements of excitation function of the total fission cross sections in reverse kinematics, with an experimental setup ensuring a complete transmission of the fission fragments, would help to clarify the situation.

3.6 Shapes of the isotopic and isobaric distributions

As already noticed in section 3.1, the mean value and the width of the isotopic distributions evolve with the element charge. Actually, they depend on the N/Z ratio and on the excitation energy of the fissioning system. This can be seen more clearly in Fig. 16 where the ratio of the mean neutron number over the charge Z and standard deviations of our isotopic cross-section distributions have been represented together with $^{208}Pb + p$ (1000 A MeV) and $^{208}Pb + d$ (1000 A MeV) results as a function of the charge. In the upper part of the Fig. 16 it can be seen that the fission fragments produced in the reaction $^{208}Pb + p$ (500 A MeV) are mainly neutron-rich while the fragments resulting from the fission of the system $^{208}Pb + p$ (1000 A MeV) are nearer the valley of stability (black line, average values taken from [53]) and even on the neutron-deficient side. The data for $^{208}Pb + d$ (1000 A MeV) are even more neutron-deficient. These features can be understood in terms of the imparted excitation energies in the primary residuals which increase with the bombarding energy. The fact that for increasing Z, the fission fragments become more neutron-deficient is due to the excitation energy sharing between them. If the N/Z ratio at separation is the same as the one of the fissioning system as in the hypothesis

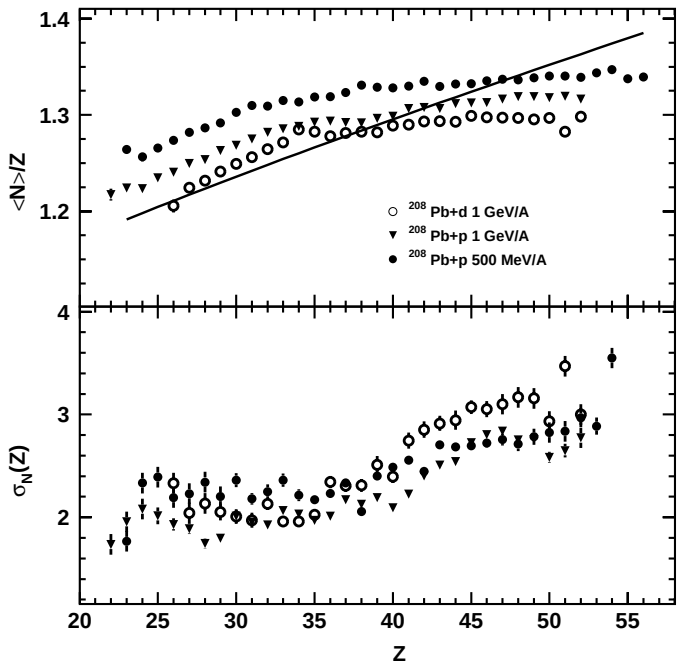

Figure 16. *Upper panel: Ratio between the mean neutron number and the charge as a function of the atomic number. The black line corresponds to the stable isotopes [53]. Bottom panel: standard deviation of the isotopic distribution as a function of the atomic number. The error bars are given by the uncertainty of the fit.*

of unchanged charge density (UCD) [52], and if the excitation energy sharing is proportional to the masses as in the equal temperature assumption, the heaviest fragments will evaporate more neutrons.

The width of the isotopic distributions increases slightly with Z at a given energy, particularly in the region with $Z > 40$. This again reflects the fact that more neutrons are evaporated from heavier fragments, leading consequently to more fluctuations. As regards to the dependence with incident energy, only the 2 GeV data show a significative increase of the widths.

To compare with previous data we have also plotted in Fig. 17 (upper panel) the N/<Z> ratio as a function of mass, with N = A-<Z>. The agreement with the data of Hagebo et al. [46] measured at ISOLDE at 600 MeV is good up to A=105. Beyond, our data seem to populate more neutron-rich nuclei. This could be explained by the higher energy used in [46], the heavier fragments evaporating more neutrons. A few data for a neighboring system $^{208}Bi + p$ at 450 MeV [54] are also shown, which are perfectly consistent with the present measurements. The width (standard deviation) of the isobaric distributions

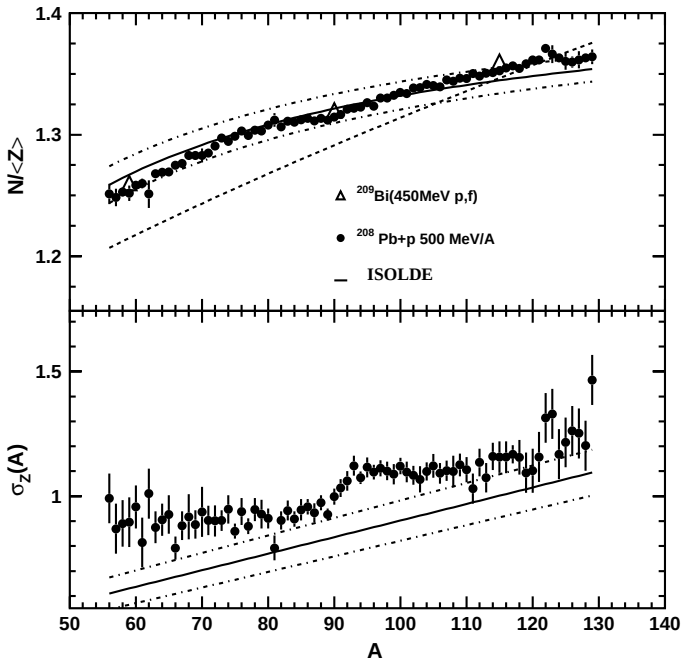

Figure 17. *Upper panel: Ratio between the neutron number and the mean fragment charge as a function of the mass. The dashed line corresponds to the stable isotopes [53]. The meaning of the symbols is given in the figure. Bottom panel: standard deviation of the charge distribution as a function of the mass. The error bars are given by the uncertainty of the fit. In both panels, the full lines are the systematics of ref.[46] and the dashed-dotted lines their dispersions.*

versus the mass from Hagebo et al. and our experiment are compared in the lower panel of the same figure. Both data show an increase with the mass but the ISOLDE data [46] are systematically lower. The reason is probably the fact that in the present work, a larger number of elements for each mass is accessible to measurements.

4 Kinematical properties of the fission fragments

4.1 Velocity distributions

In the present experiment, the longitudinal momenta of the isotopes were also measured, which provide information on the kinematical properties of the fission fragments. A complete survey of the velocity distributions, in the lead rest frame, integrated over all the masses as a function of the nuclear charge

is represented in Fig. 18. In the left panel, the measurements obtained with the hydrogen target, i.e. for reactions of ^{208}Pb on $Ti + H_2$, are shown. Three components can be seen: one for heavy fragments with velocities centered around zero and two symmetrical wings, in which the absolute value of the velocity decreases with increasing Z. The last ones corresponds to fission-fragment velocity distributions cut by the acceptance of the FRS, as discussed in sect. 2.6.1. The first component is totally due to evaporation residues coming from reactions on the target windows, since it disappears (right panel) when the contribution from the dummy target (middle panel) is subtracted. This means that at 500 A MeV the excitation energy in the reaction $^{208}Pb + H_2$ is not high enough to produce an appreciable number of evaporation residues down to Z=57.

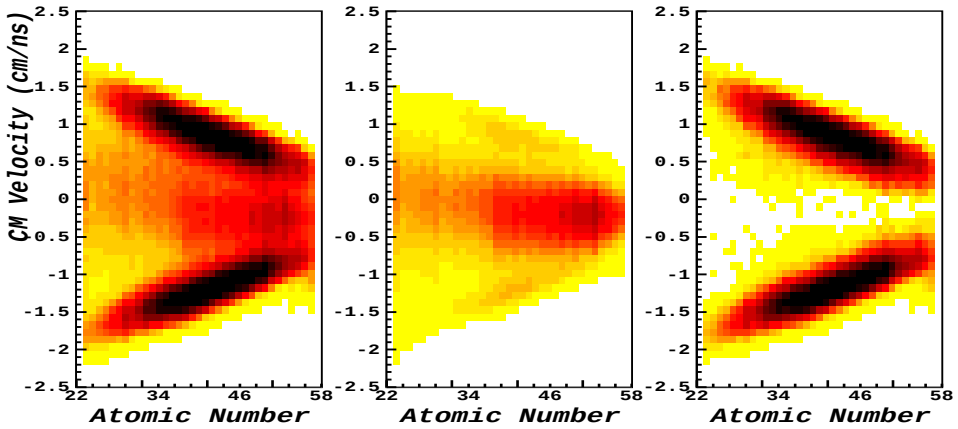

Figure 18. *Two-dimensional plots of the average velocity in the lead rest frame versus the atomic number. Left: Data obtained with the full target. Middle: The measured velocities in the dummy target. Right: Data extracted for the* ^{208}Pb *+ p reaction.*

To deduce the average velocities of the fission fragments from the measured velocities, we took into account the angular cuts. The average values of the transmission-corrected velocity distributions for each element integrated over the isotope masses are shown in Fig. 19. The corrected experimental velocity values are also tabulated in table 11 in the appendix.

4.2 Reconstruction of the fissioning system.

From the average properties of the fission fragments we can try to trace back the characteristics of the fissioning nucleus. This can be done by using the charge and mass distributions and the correlation between the charge and the velocity of the fragments. Since the fission fragments can still be excited at the scission point, they are detected after eventual evaporation. In the present reconstruction we will take into account this post-scission emission.

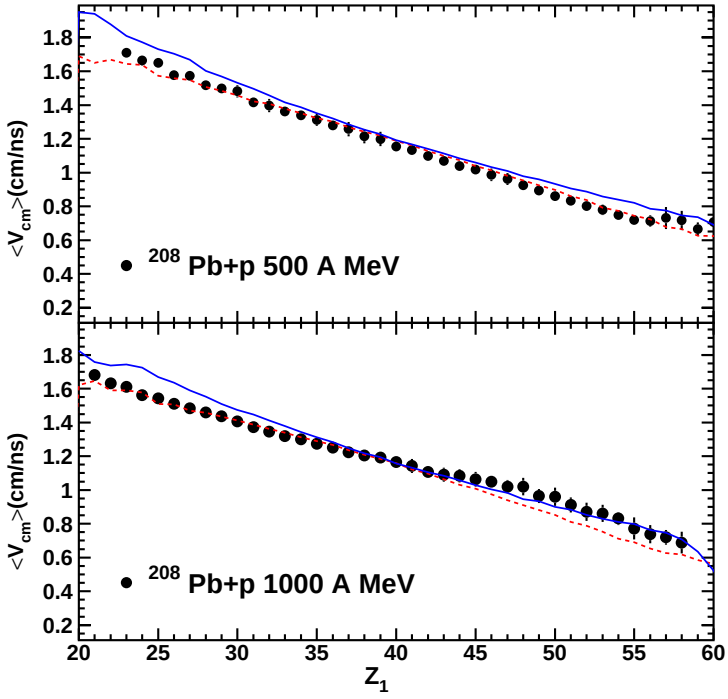

Figure 19. *Fission fragment recoil velocities in the lead rest frame as a function of the fragment charge. The lines are the results of calculations using the INCL4+ABLA (dashed lines), and the INCL4+GEM (solid lines) codes (see section 5.2.2). Points are data at 500 MeV (upper part, this work) and at 1000 MeV (lower part, [4]). The uncertainties are shown if they exceed the size of the symbols.*

First, we can directly deduce the average value of the charge of the fissioning system, Z_{fis}, from twice the mean value of the charge distribution of the fission fragments, $< Z >$. Indeed, our charge identification was carried out without any ambiguity (see sections 2.3, 2.4) and it can be assumed, as also predicted by calculations (see section 5), that the fission fragments have not evaporated charged particles, since they are mostly neutron-rich and their excitation energy is rather small. The statistical uncertainty being negligible, the uncertainty on the determination of Z_{fis} is only due to possible systematical uncertainties on relative values of cross-sections. As discussed before, the relative uncertainties are very small except for the tails of the distributions which contribute only negligibly to the average Z value. Therefore, the determination of the mean nuclear charge of the fissioning system is rather precise:

$$Z_{fis} = 2* < Z >= 80.0 \pm 0.2 \tag{11}$$

The mass of the fissioning system, A_{fis}, cannot be deduced using the same method because of the post-fission neutron evaporation. From the measured

isotopic distributions in Fig. 11, we can determine for each fission element Z_1 the mean mass value $< A_1 >_{post} (Z_1)$ detected after neutron evaporation.

The total kinetic energy, TKE, of the two fission fragments before neutron emisssion in the fissioning system is:

$$TKE = \frac{1}{2} m_0 < A_1 >_{pre} v_1^2 + \frac{1}{2} m_0 < A_2 >_{pre} v_2^2 \tag{12}$$

in which $v_1, v_2, < A_1 >_{pre}, Z_1, < A_2 >_{pre}, Z_2$ denote respectively the velocities in the fissioning system, the masses before neutron evaporation and charges of the two fission fragments. It is given to a good approximation by the Coulomb repulsion force at scission:

$$TKE = \frac{Z_1 Z_2 e^2}{D} \tag{13}$$

where D can be taken from the systematics of [55, 56, 57] established on experimental measurements of TKE on a large variety of systems:

$$D = r_0 < A_1 >_{pre}^{\frac{1}{3}} \left(1 + \frac{2\beta}{3}\right) + r_0 < A_2 >_{pre}^{\frac{1}{3}} \left(1 + \frac{2\beta}{3}\right) + d \tag{14}$$

with $r_0 = 1.16\ fm$, $\beta = 0.625$ and $d = 2\ fm$.

The momentum is conserved in the fission process, therefore:

$$< A_1 >_{pre} v_1 =< A_2 >_{pre} v_2 \tag{15}$$

The mean value of the fission fragment mass before neutron emission, $< A >_{pre} (Z)$, can be obtained from the measured mass $< A >_{post} (Z)$ as:

$$< A_i >_{pre} (Z_i) =< A_i >_{post} (Z_i) + \bar{\nu}_{ipost} \tag{16}$$

where $\bar{\nu}_{ipost}$ represents the number of neutrons evaporated in average by the fission fragment denoted by i.

The excitation energy of the prefragment can be assumed to be distributed proportionally to the masses of the fission fragments at the scission point. Since the total number of evaporated neutrons, $\bar{\nu}_{post}$, is roughly proportional to the excitation energy, the number of neutrons evaporated by each fragment $\bar{\nu}_i$ is defined by:

$$\bar{\nu}_{ipost} = \frac{< A_i >_{pre}}{< A_1 >_{pre} + < A_2 >_{pre}} * \bar{\nu}_{post} \tag{17}$$

We will assume that a similar relation also holds for the masses after neutron evaporation, $< A_i >_{post}$. It has been checked through a simulation with the INCL4/ABLA model that this leads to an error on $\bar{\nu}_{post}$ always smaller than 0.5%.

For a fixed charge of the fissioning system, combining the equations 17 for $< A_i >_{post}$, 16, 15 and 13, we get a function that relates the charge, the measured mean mass and the mean velocity of fission fragments, for a given value of the number of post-fission evaporated neutrons, $\bar{\nu}_{post}$. In our case, the charge of the fissioning system is fixed to $Z_{fis} = 80.0$ and $\bar{\nu}_{post}$ is a free parameter to be determined.

$$v_1 = f(< A_1 >_{post}, Z_1, \bar{\nu}_{post}, Z_{fis} = 80.0) \tag{18}$$

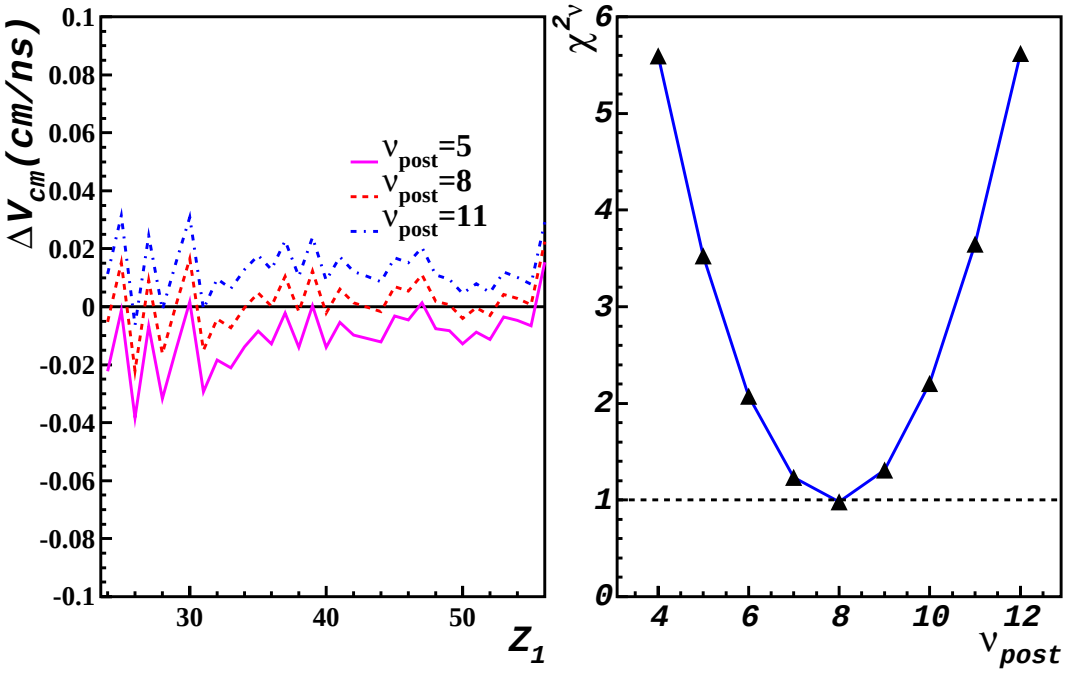

Figure 20. *Left: differences ΔV_{cm} between the experimental average velocities in the center-of-mass system (see table 11) and calculations assuming different numbers of post-fission neutrons, as a function of the nuclear charge. The different lines correspond to the different velocity values calculated with $\bar{\nu}_{post} = 5$ (full line), $\bar{\nu}_{post} = 8$ (dashed line), $\bar{\nu}_{post} = 11$ (dashed-dotted line). Right: Variation of the χ^2 by degree of freedom as a function of the number of evaporated neutrons.*

If all the fission fragments come in average from the same Z_{fis} of the fissioning nucleus, then the average values for each Z of the experimental and calculated

velocities value should be equal when the assumed $\bar{\nu}_{post}$ number of post-fission evaporated neutrons corresponds to the actual number. This is what is shown in Fig.20 left) where the velocity difference, corresponding to different values of $\bar{\nu}_{post}$, is represented as a function of the nuclear charge. It can be seen that with $\bar{\nu}_{post} = 8$ the velocity difference as a function of the fragment charge is compatible in average with 0. This confirms that the fission fragments do not originate from very different Z_{fis}, although fluctuations appear, probably due to smaller statistics, for low Z. In order to determine the best fit to the data with equation 18, the χ^2 has been calculated as a function of the number of post-fission emitted neutrons and shown in the Fig. 20 right).The minimum is reached for $\bar{\nu}_{post} = 8$. The uncertainty on this value due to the one on $< Z_{fis} >$ is ± 1.5. With the error on the fit procedure and possible uncertainty on the value of D in equation 14, we estimate the total uncertainty to ± 3. The present result

$$\bar{\nu}_{post} = 8.0 \pm 3 \tag{19}$$

is in very good agreement with the one obtained by Z. Fraenkel et al. [58], $\bar{\nu}_{post} = 7.20 \pm 1.44$ for the reaction $^{209}Bi+p$ at 475 MeV. Furthermore, the number of neutrons emitted post-fission estimated with the code INCL4/ABLA [20] is compatible with our result: $\bar{\nu}^{calc}_{post} = 10 \pm 2$.

The mass of the fissioning system $< A_{fis} >$ can therefore be obtained from:

$$< A_{fis} >= 2 * < A >_{post} + \bar{\nu}_{post} = 186 + 8 = 194 \pm 3.8 \tag{20}$$

As was done in [59], we can also try to derive from our results the excitation energy at the saddle point. According to [52], it is related to the width of the charge distribution, σ_Z, by the following expression:

$$\sigma_Z^2 = \frac{1}{2} \frac{\sqrt{E^*_{Bf}}}{\sqrt{a} C_{mac}} \tag{21}$$

where E^*_{Bf} is the excitation energy above the fission barrier, a is the level density parameter and C_{mac} is the curvature of the macroscopic potential V_{mac} as a function of charge asymmetry at the saddle point:

$$C_{mac} = \frac{8}{Z^2_{fis}} \frac{d^2 V_{mac}}{d\eta^2} \tag{22}$$

where $\eta = \frac{4}{A_{fis}}(A - \frac{A_{fis}}{2})$ is the asymmetry term, A_{fis} and Z_{fis} are the mass

and charge of the fissioning system respectively and A the fission-fragment mass. Since at high excitation energy shell and pairing effects are expected to disappear [60], we have used the asymptotic value of the level density parameter from [61]. The curvature C_{mac} from the potential V_{mac} is obtained from a fit to the experimental data on mass distributions of fission fragments [61, 62]. From this systematics, the second derivative of the potential at the fission barrier for our values of $< Z_{fis} >$ and $< A_{fis} >$ is $\frac{d^2V_{mac}}{d\eta^2} = 23$.

Inserting the measured width of the charge distribution, $\sigma(Z) = 6.3 \pm 0.2$ from section 3.4, in the equation 21, we get the excitation energy above the fission barrier, $E^*_{Bf} = 93 \pm 12$ MeV. If we take the value of the fission barrier, $B_f = 14$ MeV [63], the total excitation energy in the system is in average

$$E^*_{tot} = 107 \pm 22 MeV. \tag{23}$$

The error bar on this quantity is rather large. First because equation 21 is strictly valid if the Z-distribution has a gaussian shape, which is not completely true in our case likely because it corresponds to a distribution of fissioning nuclei with a distribution of excitation energy. Second, the extraction of E^* is dependent on the parameters used in equations 21 and 22. From the obtained excitation energy above the fission barrier and assuming that in average 10 MeV is needed to evaporate one neutron, we can estimate a number of post-fission neutrons $\bar{\nu}_{post} = 9.3 \pm 2.$, which is consistent with the previous results.

4.2.1 Average kinetic energy of fission products

In the hypothesis of an isotropic velocity distribution, the kinetic energy of the fission fragments in the lead rest frame can be calculated by using the following expression:

$$E_k^{post} = \frac{1}{2} A_f^{post} m_0 v_{cm}^2 \tag{24}$$

where A_f^{post} is the measured mass for a given isotope, m_0, the mass atomic unit, and v_{cm}, the velocity of the fragments. Here we neglect the motion of the fissioning nucleus in the lead rest frame.

In order to obtain the kinetic energy of the primary fission fragments, it is necessary to take into account the post-fission emitted neutrons. It can be assumed that the average kinetic energy per nucleon is conserved, so that:

$$< E_k^{pre} >= \frac{A_f^{pre}}{A_f^{post}} E_k^{post} = \frac{A_f^{post} + \bar{\nu}_f^{post}}{A_f^{post}} E_k^{post} \tag{25}$$

where $\bar{\nu}_f^{post}$ is the average neutron number emitted by the fragment calculated with the help of expression 17.

Z	A	$E_k^{pre}(MeV)$	T(MeV)
46	103	54.7 ± 2.6	58.9 ± 1.7
46	109	55.3 ± 2.7	56.5 ± 1.9
46	112	50.9 ± 2.5	54.6 ± 1.3
47	111	52.5 ± 2.6	57.4 ± 1.6
47	112	54.4 ± 2.7	56.8 ± 2.1
47	113	52.9 ± 2.6	53.6 ± 1.4
49	111	47.5 ± 2.4	54.2 ± 1.3

Table 4
Kinetic energies in the center-of-mass system corrected for neutron evaporation, (E_k^{pre}) compared to those measured by [64] (T) for different isotopes. The uncertainty quoted for T is only the experimental one. According to [64], an additional uncertainty of about 5% should be applied in order to account for some further corrections.

We can then compare the E_k^{pre} values obtained with this procedure to p+ ^{208}Pb data at 450 MeV obtained for a few isotopes by Panontin and Porile [64]. Our uncertainty has been estimated to about 5%, coming from the uncertainty on the determination of the experimental velocities and the uncertainties on the number of emitted neutrons. The comparison is displayed in table 4. Within the uncertainties, all the compared data are compatible, with the exception of the ^{111}In isotope, where the discrepancy reaches 15%.

The most probable total kinetic energy of the fragments deduced from the present data is $< TKE >= 134 \pm 5$ MeV. This value is in good agreement with the systematics of [65, 66], which gives for a fissioning system having $Z_{fis} = 80$ and $A_{fis} = 194$, $< TKE >= 139 \pm 3$ MeV. Furthermore, this $< TKE >$ value inserted in eq. 13, gives a value for the parameter D very close to the one deduced from eq. 14.

5 Comparison with models

This section deals with the comparison of the experimental data with well-known spallation codes. As said in the introduction, generally the reaction is viewed as a two-step process, an intra-nuclear cascade stage leading to an excited nucleus, followed by evaporation and/or fission. Therefore, the codes describing the reaction generally couple two different approaches, an INC model and a statistical de-excitation one. Here, we will compare the experi-

mental results either with two different intranuclear-cascade models, namely ISABEL [67] and INCL4 [20], followed by the same evaporation-fission approach, the ABLA model from [23, 24], for observables more related to the first step of the reaction or with INCL4 followed by two different deexcitation models, ABLA and GEM [25], for quantities more dependent on this stage. Actually, none of these combinations of models is able to reproduce the total fission cross-section obtained experimentally, therefore we will mainly concentrate on comparisons to the shapes of the different distributions we measured, renormalising the calculations with respect to the experimental data when cross-sections will be concerned.

5.1 Properties of the fissioning system

The intranuclear-cascade stage determines the initial conditions for the deexcitation. The competition between fission and evaporation and between the different types of evaporated particles depends on the charge, mass, excitation energy and angular momentum of the excited system. Fission generally occurs, as predicted by the calculations, before the evaporation of charged particles that would decrease the fissility parameter, Z^2/A. In section 4.2, we have reconstructed the properties of the fissioning system. We can here compare them with the results of two calculations using either ISABEL or INCL4 for the INC stage, followed by the same ABLA model. Actually, the combination INCL4/ABLA has been shown to rather well reproduce fission distributions in the case of Au+p at 800 A MeV and Pb+p at 1 A GeV [20]. In the first three lines of table 5, the mean value of the fissility parameter $(Z^2/A)_{fis}(Exp)$ of the fissioning nucleus, i.e. **after pre-fission evaporation**, calculated with the value of Z_{fis} and A_{fis} obtained respectively in eqs. 11 and 20 is compared to the values obtained with the two INC codes, resp. $(Z^2/A)_{fis}(INCL4)$ and $(Z^2/A)_{fis}(ISABEL)$. Note that here pre-fission evaporation actually means pre-saddle evaporation but the decision for fission as well as the characteristics of the fission fragments will not be changed by the descent from saddle to scission. The two models give the same value in good agreement with the experimental result.

Also shown in the same table is the excitation energy, E^*_{fis}, just before fission, deduced from the experiment through equation 23 and from the models. Actually, the values given by the models depends on the choice of the dissipation coefficient, β in the ABLA model. A change of β from 1.5 (standard value used in [20]) to 2.0 10^{21} s^{-1} (value recommended in [59]) leads to a decrease of the pre-fission excitation energy by about 15% (while the isotopic, mass and charge distributions are not affected). This, together with the rather large uncertainty on the experimental value, only permits to say that the models and the experiment are compatible.

In the same table we have also shown the mean values of the fissility parameter and excitation energy of the nuclei that will fission at the end of INC, **before evaporation**, $(Z^2/A)_{casc}$ and E^*_{casc}. It can be seen that, during the pre-fission evaporation, almost half of the excitation energy is dissipated and that the fissility parameter increases indicating that mostly neutrons are evaporated.

The other columns of table 5 give the same informations for the two other reactions studied at GSI, Pb+p 1000 MeV [4] and Pb+d 2000 MeV [5]. An estimation of the experimental excitation energies for these two systems have been obtained in the same way as for 500 MeV, assuming a number of post-fission neutrons of, respectively, 10 and 14 for 1000 and 2000 MeV. The uncertainties have been increased to take into account this assumption and the fact that it becomes less justified to neglect post-fission charged particle evaporation, especially at 2000 MeV. The same trends as at 500 MeV can be observed. A tendency is visible for the increase of the mean excitation energy of the fissioning nucleus with the incident energy, a fact which is also reflected by the calculations. They also show that the involved excitation energies at the end of the cascade are much larger, leading consequently to a more important evaporation. As at 500 MeV, the fissility parameter is the same in the two INC models while E^* is always larger with ISABEL, the difference increases with increasing incident energy. A higher E^* at the end of the intranuclear cascade had been previously observed in [68] where it has been suggested that it could come from differences in the treatment of the Pauli blocking or of the pion production. Actually ISABEL emits less nucleons than INCL4, a fact which may be due to the difference in the criterium for stopping the intranuclear cascade in the codes. However, here the average E^* for fission events also depends on the evaporation/fission model that decides which nuclei will undergo fission according not only to their excitation energies and fissility but also angular momentum which is higher in INCL4 than in ISABEL.

The width of the experimental charge distribution can also be directly compared to the predictions of the models. In Fig. 21, the mean values of the charge distribution width measured experimentally for the three systems, 500 MeV $^{208}Pb+p$, 1000 MeV $^{208}Pb+p$ [4], 2000 MeV $^{208}Pb+d$ [5], are compared with calculations with ISABEL and INCL4 coupled to ABLA. It can be seen that a slightly better agreement is found between the experimental values and the results of the INCL4 model. ISABEL reproduces quite well the trend of the charge distribution width with the energy, however the absolute values are somewhat overestimated. Due to the large uncertainties on the deduced excitation energies, the measured charge widths could be more reliable for the comparison between data and calculations. The interplay between the excitation energy at the end of the INC stage, the angular momentum and the fissility parameter seems better predicted when using the INCL4-ABLA combination. The calculated widths are larger than the experimental ones even if the predicted mean excitation energies are smaller than those deduced from

Reaction	^{208}Pb+p 500 MeV	^{208}Pb+p 1000 MeV	^{208}Pb+d 2000 MeV
$(Z^2/A)_{fis}(Exp)$	33.1 ± 0.5		
$(Z^2/A)_{fis}(INCL4)$	33.4	32.9	32.1
$(Z^2/A)_{fis}(ISABEL)$	33.4	32.9	32.1
$(Z^2/A)_{casc}(INCL4)$	32.8	32.4	31.8
$(Z^2/A)_{casc}(ISABEL)$	32.8	32.5	32.1
$E^*_{fis}(Exp)$	107± 22	120± 35	150± 45
$E^*_{fis}(INCL4)$	86	110	138
$E^*_{fis}(ISABEL)$	103	132	164
$E^*_{casc}(INCL4)$	160	218	291
$E^*_{casc}(ISABEL)$	201	278	393

Table 5
Mean values of the fissility parameter Z^2/A, and excitation energies in MeV, E^*, deduced from the present experiment and calculated with the ISABEL and INCL4 INC models followed by the same evaporation/fission, ABLA. The subscript "fis" means values for the fissioning nucleus after pre-fission evaporation while "casc" means at the end of the cascade stage for remnants that will undergo fission.

the data. This fact tends to indicate that equation 21 is not fulfilled in the calculations. Beyond the mean values, the predicted distributions of variables like the fissility parameters or the excitation energies whould have to be compared to experiments. However, this task is beyond the possibility of the present single data and will require further exclusive experiments.

5.2 Influence of the different de-excitation approaches

Here, we have adopted INCL4 as the INC model and we study the influence of the de-excitation stage by varying the evaporation/fission model, actually taking either ABLA or the GEM model from ref. [25].

5.2.1 Shape of the isotopic distributions

For a given fissioning nucleus, the shape of the isotopic distributions is mainly influenced by the details of the evaporation/fission models, in particular, the parameterisation of the fragment mass and charge distributions and the number of evaporated particles after fission. In Fig. 11, we show a comparison between the experimental isotopic cross-sections and the results from the codes

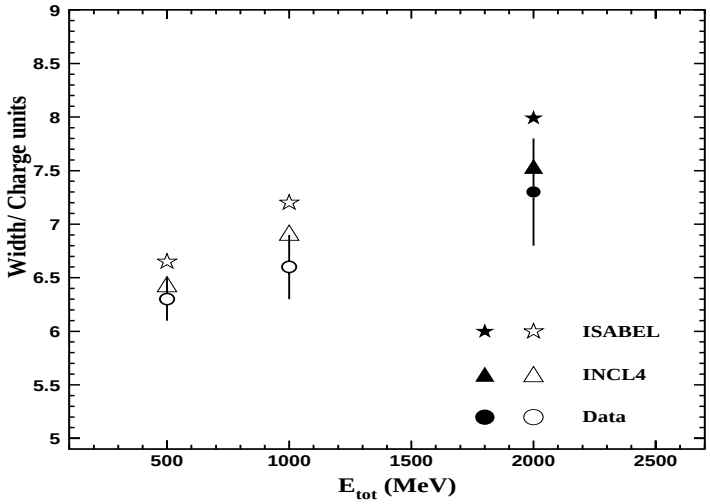

Figure 21. *Widths of the fission fragment charge distribution as a function of the total incident energy in MeV, measured (circles) in the reactions 500 MeV* $^{208}Pb+p$ *(this work), 1000 MeV* $^{208}Pb+p$ *([4]), 2000 MeV* $^{208}Pb+d$ *[5] and predicted by the ISABEL-ABLA (stars) and INCL4-ABLA (triangles). The widths have been deduced from a gaussian fit. For the calculations the fit has been made on the measured range of charges.*

INCL4+ABLA (solid line) and INCL4+GEM (dashed line), renormalised to the experimental total fission cross-section. It can be observed that both codes reproduce reasonably the experimental data, with however a little desavantage for the INCL4/GEM combination, which underestimates, in relative value, the lightest fragments. The general trends of the shapes of the distributions can be better seen in Fig. 22 that displays the mean <N>/Z and width values for each Z for the present data and the same system at 1 GeV compared with the two codes. As regards to the position of the mean value, ABLA seems to agree better than GEM for the heaviest fragments while it is the contrary for the lightest ones. Similar conclusions can be drawn at 1 GeV, although the width values present more fluctuations. It is interesting to notice that GEM exhibits relatively strong even/odd effects not observed experimentally. This could arise from the neglect of gamma emission which was claimed in [35] to wash out pairing effects for heavy nuclei. Actually, GEM was also found to predict too strong even-odd effects for the $^{56}Fe+p$ reaction in the reference [37]. It should be noted that the presently used version of ABLA does not contain shell and pairing effects nor gamma decay.

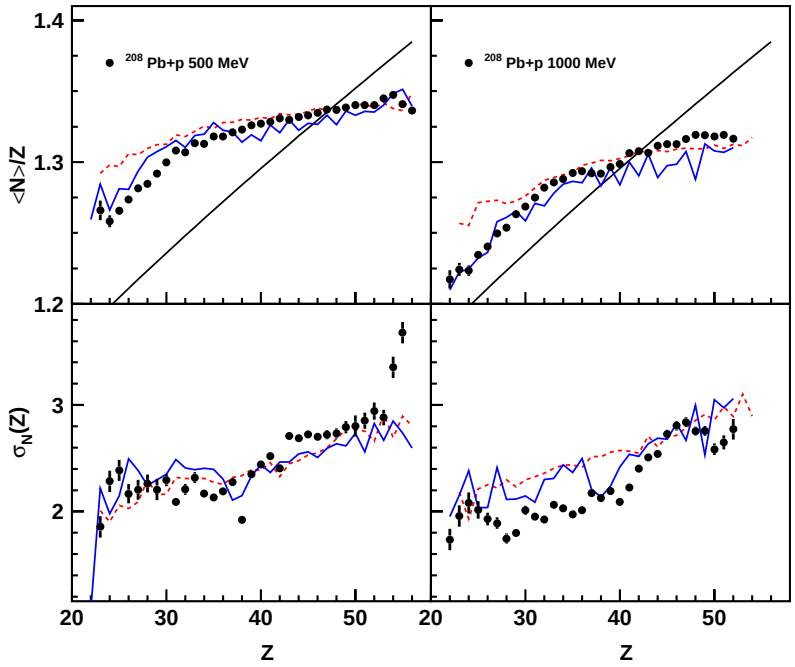

Figure 22. *Points are data at 500 MeV (left) and 1000 MeV (right). Dashed curves are results of INCL4/ABLA and full curves of INCL4/GEM calculations. Upper panels: Ratio between the mean neutron number and the charge as a function of the nuclear charge. The full line corresponds to the stable isotopes [53]. Lower panels: Standard deviations of the isotopic distribution as a function of the nuclear charge.*

5.2.2 Recoil velocities of the fission fragments

The comparison of the experimental recoil velocities of the fission fragments with the results obtained from ABLA (dashed line) and GEM (full line) codes following INCL4 for two different incident energies 500 MeV (top), and 1000 MeV [4]) (bottom) is shown in Fig. 19. At 500 MeV, the code INCL4+ABLA is in excellent agreement with the experimental data, for all charges, within always less than 3%. On the contrary the GEM calculation agrees with the experience only for middle charges, diverging significantly for the lowest and highest ones. Actually, in ABLA the recoil velocities are calculated from the Coulomb repulsion of the two fragments, according to the equation 13, while in GEM they are obtained from a parameterisation of the average and of the width of the fragment velocities based on a few available measurements. Our results give an indication that the approach chosen in ABLA leads to better predictions. In the case of the reaction at 1000 MeV, the values predicted by INCL4+ABLA are in good agreement with the measured ones up to around Z=45, above the calculation underestimates the results.

6 Conclusions

The experiment presented in this paper follows a series of studies of spallation reactions around 1 A GeV carried out at the FRS at GSI and has provided, for the first time, isotopic and velocity distributions of fission fragments produced in spallation reactions of heavy nuclei at 500 A MeV. About 400 fission fragments from the reaction ^{208}Pb+p have been fully identified in atomic and mass numbers, their isotopic production cross-sections measured and their velocity distributions reconstructed.

The present results have been compared to previous data, obtained generally in direct-kinematics measurements. The shapes of the mass, charge and isotopic distributions as well as the average kinetic energies have been found in excellent agreement with the literature data, and the isotopic cross-sections are compatible, within the error bars, to the ones measured by gamma-spectrometry. On the other hand, the total fission cross-section deduced from our data was found substancially higher than expected from systematics on previous measurements. No explanation for this discrepancy has been found. In view of the large disparity between the values obtained with different techniques, in different experiments, it seems that only a direct and precise measurement of total fission cross-sections as a function of energy would help to clarify the situation.

The comparison to previous FRS data has allowed to study the incident-energy dependence of the isotopic distribution shapes. It was found that when increasing the incident energy the produced fragments are less neutron-rich and the distribution widths are larger, reflecting the increase of the excitation energy in the fissioning system.

The combined measurement of all the fission fragments with their velocity distribution makes it possible to reconstruct the average fissioning system. Assuming that the average charge of the fissioning system is directly given by our measured charge distribution, we show that the number of post-fission neutrons can be inferred. The result obtained is $< \nu_{post} >= 8 \pm 3$ which is in good agreement with previous publications. The characteristics of the average fissioning system can then be deduced. The mass and charge of the fissioning system are found $< A_{fis} >= 194 \pm 3.8$ and $< Z_{fis} >= 80.0 \pm 0.2$ respectively. The obtained value for the mean excitation energy $< E^*_{tot} >= 107 \pm 22 MeV$ is consistent with the deduced $< \nu_{post} >$ number.

The experimental data have been compared to the results of the different combinations of INC and evaporation/fission models describing the spallation reaction (with a renormalisation of the model total fission cross-section to our value). From the comparison of the charge-width distribution with two

different INC models, it was found that the INCL4 model provides slightly better results than ISABEL, probably due to the differences in excitation energy release and angular momenta at the end of the intranuclear-cascade stage. The test of the two statistical de-excitation models GEM and ABLA coupled to the same intranuclear code over all the observables shows a better agreement with the code ABLA developed at GSI for the present discussed fission characteristics. The models are also shown to follow reasonably well the evolution of the shapes of the distributions with the incident energy from 500 to 1000 MeV. To go further in the understanding of the reaction mechanism, and in particular to better disentangle the respective role of the two stages of the spallation reactions, more exclusive experiments [69] measuring paricles in coincidence with the fragments would be needed.

References

[1] J. Benlliure, et al., Nucl. Phys. A 683 (2001) 513.
[2] F. Rejmund, et al., Nucl. Phys. A 683 (2001) 540.
[3] W. Wlazlo, et al., Phys. Rev. Lett. 84 (2000) 5736.
[4] T. Enqvist, et al., Nucl. Phys. A 686 (2001) 481.
[5] T. Enqvist, et al., Nucl. Phys. A 703 (2002) 213.
[6] J. Taieb, et al., Nucl. Phys. A 724 (2003) 413.
[7] M. Bernas, et al., Nucl. Phys. A 725 (2003) 435.
[8] Spallation neutron source (SNS) CDR Report (NSNS/CDR-2), 1997. http://www.ornl.gov/nsns/CDRDocuments/CDR.html.
[9] The European Spallation Source study. The ESS Technical Study, report ESS-96-53-M III, 1996.
[10] C. D. Bowman, et al., Nucl. Inst. Meth. A 320 (1992) 336.
[11] C. Rubbia, et al., rapport CERN/AT/93-47/(ET) 1993.
[12] C. Rubbia, et al., rapport CERN/AT/95-44/(ET) 1995.
[13] W. F. Henning. Nucl. Inst. Meth. B 126 (1997) 1.
[14] R. Rossi, et al., Z. Phys. 82 (1933) 151.
[15] R. Michel, et al., Nucl. Inst. Meth. B 129 (1997) 153.
[16] M. Gloris, et al., Nucl. Inst. Meth. A 463 (2001) 593.
[17] G. S. Bauer, et al., J. Nucl. Mater. 296 (2001) 17.
[18] H. Aït Abderrahim et al., proceedings of the Int. Workshop on P&T and ADS development, SCK-CEN, October 6-8, 2003 Mol, Belgium.
[19] R. Serber, Phys. Rev. 72 (1947) 1114.
[20] A. Boudard, et al., Phys. Rev. C 66 (2002) 044615.
[21] S. G. Mashnik and A. J. Sierk Proceedings of the Fourth International Topical Meeting on Nuclear Applications of Accelerator Technology (AccApp00), Washington, DC 2000. (American Nuclear Society, La Grange Park, IL, 2001) p.328.
[22] H. Duarte Proceedings of the Fifth Workshop On Simulating Accelerator

Radiation Environments (SARE-5) Paris July 17-18, 2000. D. Filges, F. Goldenbaum and Y. Yariv Editors, ESS 112-01.T, p.83.
[23] J. J. Gaimard and K.-H. Schmidt, Nucl. Phys. A 531 (1991) 709.
[24] A. R. Junghans, et al., Nucl. Phys. A 629 (1998) 635.
[25] S. Furihata, Nucl. Inst. Meth. B 171 (2000) 251.
[26] S. G. Mashnik, et al., Proceedings of the Workshop on Nuclear Data for the Transmutation of Nuclear Waste, GSI-Darmstadt, Germany, September 1-5, 2003, ISBN 3-00-012276-1, edited by Aleksandra Kelic and Karl-Heinz Schmidt. http://www-wnt.gsi.de/tramu/.
[27] L. Audouin, PhD Thesis at IPN, Orsay 30/9/2003 and in preparation.
[28] H. Geissel, et al., Nucl. Inst. Meth. B 70 (1992) 286.
[29] K.-H. Schmidt, et al., Nucl. Inst. Meth. A 260 (1987) 260.
[30] B. Jurado, et al., Nucl. Inst. Meth. A 483 (2002) 603.
http://www-w2k.gsi.de/kschmidt/seetraminfo/calibration.htm.
[31] P. Chesny, et al., Annual report GSI p190, 1996.
[32] B. Voss, et al., Nucl. Inst. Meth. A 364 (1995) 150.
[33] M. Pfützner, et al., Nucl. Inst. Meth. B 86 (1994) 213.
[34] H. Stelzer, Nucl. Inst. Meth. A 310 (1991) 103.
[35] M. V. Ricciardi, et al., Nucl. Phys. A 733 (2004) 299.
[36] B. Fernandez, PhD Thesis at DAPNIA/SPhN CEA, Saclay 14/3/2003.
[37] C. Villagrasa, PhD Thesis at DAPNIA/SPhN CEA, Saclay 5/12/2003.
[38] J. Benlliure, J. Pereira-Conca and K-H Schmidt, Nucl. Inst. Meth. A 478 (2002) 493.
[39] C. Scheidenberger, et al., Nucl. Inst. Meth. B 141 (1998) 441.
[40] http://www-wnt.gsi.de/kschmidt/amadeus.htm.
[41] P. J. Karol, Phys. Rev. C 11 (1975) 1203.
[42] P. Napolitani, et al., Nucl. Phys. A 727 (2003) 120.
[43] A. V. Prokofiev, Nucl. Inst. Meth. A 463 (2001) 557.
[44] Yu. E. Titarenko, et al., Phys. Rev. C 65 (2002) 064610.
[45] Yu. E. Titarenko, et al., Proceedings of the 7th Meeting of the Expert Group on Shielding Aspects of Accelerators, Targets and Irradiation Facilities, SATIF-7, 17-18 May 2004, ITN, Savacem, Portugal.
[46] E. Hagebo and T. Lund, J. inorg. nucl. Chem. 37 (1975) 1569.
[47] L. A. Vaishnene, et al., Z. Phys. A 143 (1981) 148.
[48] X. Ledoux, et al., Phys. Rev. C 57 (1998) 2375.
[49] B . C. Barashenkov, Cross-Sections of Interactions of Particles and Nuclei with Nuclei, JINR publications, Dubna, 1993.
[50] R. Vandenbosch and J. R. Huizenga, Nuclear Fission. Academic Press New York and London 1973, p181.
[51] R. W. Hasse and W. D. Myers, Geometrical Relationships of Macroscopic Nuclear Physics. Springer-Verlag Berlin 1988, p100.
[52] P. Armbruster, Nucl. Phys. A 140 (1970) 385.
[53] P. Marmier and E. Sheldon, Physics of Nuclei and Particles. Academic Press, 1969.
[54] J. Kruger and N. T. Sugarman, Phys. Rev. 99 (1955) 1459.

[55] B. D. Wilkins, et al., Phys. Rev. C 14 (1976) 1027.
[56] C. Böckstiegel, et al, Phys. Lett. B 398 (1997) 259.
[57] K H. Schmidt, et al., Nucl. Phys. A 665 (2000) 221.
[58] Z. Fraenkel, et al., Phys. Rev. C 41 (1990) 1050.
[59] J. Benlliure, et al., Nucl. Phys. A 700 (2002) 469.
[60] A. V. Ignatyuk, et al., Nucl. Phys. A 593 (1995) 519.
[61] I. Mulgin, K.-H. Schmidt, A. Grewe and S. V. Zhdanov, Nucl. Phys. A 640 (1998) 375.
[62] A. Ya. Rusanov, M. G. Ithis, and V. N. Okolovich, Yad. Fiz. 60 (1997) 773. (Phys. At. Nucl., 60 (1977) 683).
[63] A. J. Sierk, Phys. Rev. C 33 (1986) 2039.
[64] J. A. Panontin and N. T. Porile, J. inorg. nucl. Chem. 30 (1968) 2891.
[65] V. E. Viola Jr., Nucl. Data Tables A 1 (1966) 391.
[66] V. E. Viola, K. Kwiatkowski and M. Walker, Phys. Rev. C 31 (1985) 550.
[67] Y. Yariv and Z. Fraenkel, Phys. Rev. C 20 (1979) 2227.
[68] S. Leray, et al., Proceedings of the Monte Carlo 2000 Conference, Lisbon October 23-26, 2000, p.1111
[69] J. E. Ducret, et al., Proposal S248 GSI, 2000.

7 Appendix.

Z	A	$\sigma(mb)$	Z	A	$\sigma(mb)$	Z	A	$\sigma(mb)$
23	50	0.121(0.010)(0.016)	27	61	0.757(0.018)(0.113)	30	73	0.391(0.050)(0.057)
23	51	0.190(0.013)(0.029)	27	62	0.596(0.022)(0.075)	30	74	0.180(0.038)(0.026)
23	52	0.228(0.031)(0.028)	27	63	0.564(0.022)(0.071)	31	66	0.053(0.002)(0.011)
23	53	0.209(0.050)(0.028)	27	64	0.358(0.018)(0.049)	31	67	0.260(0.004)(0.034)
23	54	0.128(0.039)(0.017)	27	65	0.223(0.016)(0.031)	31	68	0.526(0.008)(0.067)
24	52	0.194(0.008)(0.025)	28	60	0.191(0.005)(0.029)	31	69	1.054(0.014)(0.129)
24	53	0.251(0.016)(0.040)	28	61	0.362(0.006)(0.059)	31	70	1.456(0.021)(0.189)
24	54	0.335(0.016)(0.041)	28	62	0.639(0.014)(0.088)	31	71	1.680(0.028)(0.208)
24	55	0.244(0.030)(0.030)	28	63	0.860(0.017)(0.112)	31	72	1.585(0.030)(0.194)
24	56	0.222(0.026)(0.027)	28	64	0.795(0.020)(0.097)	31	73	1.336(0.028)(0.238)
24	57	0.127(0.021)(0.015)	28	65	0.690(0.022)(0.085)	31	74	0.847(0.021)(0.103)
24	58	0.072(0.016)(0.009)	28	66	0.543(0.021)(0.067)	31	75	0.511(0.017)(0.063)
25	54	0.213(0.007)(0.032)	28	67	0.348(0.016)(0.044)	31	76	0.347(0.043)(0.048)
25	55	0.321(0.012)(0.056)	28	68	0.212(0.042)(0.026)	32	69	0.188(0.003)(0.023)
25	56	0.359(0.014)(0.052)	29	63	0.340(0.006)(0.051)	32	70	0.593(0.009)(0.092)
25	57	0.408(0.018)(0.053)	29	64	0.560(0.011)(0.068)	32	71	1.120(0.015)(0.165)
25	58	0.299(0.020)(0.038)	29	65	0.943(0.017)(0.115)	32	72	1.794(0.022)(0.229)
25	59	0.235(0.019)(0.034)	29	66	1.053(0.022)(0.132)	32	73	2.086(0.028)(0.253)
25	60	0.143(0.015)(0.019)	29	67	1.083(0.027)(0.146)	32	74	2.259(0.034)(0.282)
26	56	0.186(0.005)(0.025)	29	68	0.841(0.025)(0.108)	32	75	1.703(0.029)(0.215)
26	57	0.331(0.011)(0.042)	29	69	0.608(0.020)(0.084)	32	76	1.381(0.026)(0.170)
26	58	0.473(0.013)(0.059)	30	64	0.127(0.003)(0.019)	32	77	0.796(0.038)(0.120)
26	59	0.486(0.016)(0.068)	30	65	0.348(0.006)(0.061)	32	78	0.540(0.051)(0.070)
26	60	0.463(0.022)(0.058)	30	66	0.686(0.010)(0.100)	33	71	0.178(0.003)(0.022)
26	61	0.335(0.020)(0.041)	30	67	1.085(0.017)(0.137)	33	72	0.437(0.007)(0.064)
26	62	0.215(0.015)(0.027)	30	68	1.368(0.023)(0.185)	33	73	1.096(0.013)(0.146)
26	63	0.109(0.011)(0.014)	30	69	1.372(0.029)(0.190)	33	74	1.625(0.019)(0.200)
27	58	0.178(0.005)(0.028)	30	70	1.164(0.027)(0.142)	33	75	2.458(0.029)(0.299)
27	59	0.401(0.010)(0.065)	30	71	0.917(0.025)(0.126)	33	76	2.558(0.034)(0.314)
27	60	0.464(0.011)(0.056)	30	72	0.606(0.033)(0.082)	33	77	2.656(0.037)(0.327)

Table 6

The production cross-sections in millibarns of the measured isotopes, (first column). The second and the third columns represent the statistical and systematical absolute uncertainty, respectively.

Z	A	$\sigma(mb)$	Z	A	$\sigma(mb)$	Z	A	$\sigma(mb)$
33	78	1.764(0.029)(0.218)	36	80	1.552(0.017)(0.215)	38	88	4.881(0.050)(0.600)
33	79	1.238(0.024)(0.151)	36	81	2.508(0.025)(0.320)	38	89	4.027(0.048)(0.499)
33	80	0.774(0.080)(0.110)	36	82	3.741(0.039)(0.475)	38	90	2.950(0.050)(0.365)
33	81	0.496(0.043)(0.060)	36	83	4.422(0.050)(0.548)	38	91	1.814(0.045)(0.222)
34	73	0.120(0.002)(0.026)	36	84	3.884(0.040)(0.473)	38	92	1.356(0.071)(0.190)
34	74	0.436(0.007)(0.073)	36	85	3.244(0.037)(0.414)	38	93	0.747(0.044)(0.099)
34	75	0.923(0.012)(0.115)	36	86	2.037(0.052)(0.288)	38	94	0.304(0.030)(0.038)
34	76	1.954(0.021)(0.260)	36	87	1.101(0.073)(0.150)	39	84	0.059(0.001)(0.007)
34	77	2.425(0.027)(0.306)	36	88	0.735(0.051)(0.120)	39	85	0.305(0.003)(0.059)
34	78	3.293(0.036)(0.405)	36	89	0.289(0.032)(0.041)	39	86	0.691(0.006)(0.085)
34	79	3.081(0.038)(0.377)	37	80	0.129(0.002)(0.018)	39	87	1.748(0.013)(0.253)
34	80	2.694(0.035)(0.347)	37	81	0.512(0.008)(0.062)	39	88	3.010(0.028)(0.371)
34	81	1.852(0.044)(0.237)	37	82	1.228(0.014)(0.178)	39	89	4.736(0.045)(0.687)
34	82	1.036(0.044)(0.155)	37	83	2.170(0.018)(0.268)	39	90	4.588(0.048)(0.565)
34	83	0.633(0.051)(0.091)	37	84	3.295(0.032)(0.408)	39	91	4.181(0.049)(0.570)
35	75	0.061(0.001)(0.012)	37	85	4.445(0.049)(0.547)	39	92	3.307(0.048)(0.410)
35	76	0.282(0.005)(0.067)	37	86	4.531(0.051)(0.583)	39	93	2.648(0.054)(0.400)
35	77	0.814(0.010)(0.105)	37	87	3.770(0.050)(0.526)	39	94	1.537(0.080)(0.201)
35	78	1.475(0.016)(0.182)	37	88	2.411(0.050)(0.312)	39	95	1.097(0.057)(0.143)
35	79	2.590(0.028)(0.324)	37	89	1.421(0.051)(0.206)	39	96	0.443(0.034)(0.055)
35	80	3.204(0.034)(0.456)	37	90	1.046(0.064)(0.155)	39	97	0.241(0.029)(0.031)
35	81	3.938(0.043)(0.502)	37	91	0.521(0.041)(0.083)	40	86	0.063(0.001)(0.011)
35	82	3.270(0.039)(0.402)	37	92	0.218(0.027)(0.030)	40	87	0.212(0.002)(0.033)
35	83	2.586(0.047)(0.346)	38	81	0.004(0.000)(0.001)	40	88	0.625(0.005)(0.078)
35	84	1.490(0.048)(0.198)	38	82	0.118(0.002)(0.024)	40	89	1.552(0.012)(0.214)
35	85	0.930(0.071)(0.140)	38	83	0.379(0.004)(0.052)	40	90	2.708(0.022)(0.329)
35	86	0.418(0.047)(0.064)	38	84	1.008(0.008)(0.161)	40	91	3.592(0.035)(0.438)
36	77	0.055(0.001)(0.010)	38	85	1.977(0.015)(0.240)	40	92	4.557(0.047)(0.600)
36	78	0.244(0.003)(0.037)	38	86	3.363(0.029)(0.476)	40	93	4.095(0.045)(0.498)
36	79	0.636(0.008)(0.082)	38	87	4.522(0.046)(0.551)	40	94	3.952(0.049)(0.514)

Table 7

The production cross-sections in millibarns of the measured isotopes, (first column). The second and the third columns represent the statistical and systematical uncertainty, respectively.

Z	A	$\sigma(mb)$	Z	A	$\sigma(mb)$	Z	A	$\sigma(mb)$
40	95	3.342(0.055)(0.456)	42	98	4.102(0.044)(0.511)	44	101	3.351(0.037)(0.445)
40	96	1.752(0.078)(0.238)	42	99	3.737(0.047)(0.470)	44	102	3.779(0.040)(0.488)
40	97	1.503(0.072)(0.248)	42	100	2.889(0.053)(0.379)	44	103	3.316(0.040)(0.405)
40	98	0.724(0.040)(0.089)	42	101	2.034(0.084)(0.430)	44	104	3.090(0.048)(0.380)
40	99	0.335(0.032)(0.057)	42	102	1.336(0.053)(0.194)	44	105	2.083(0.064)(0.282)
40	100	0.172(0.024)(0.029)	42	103	0.624(0.037)(0.083)	44	106	1.784(0.070)(0.267)
41	88	0.047(0.001)(0.007)	42	104	0.325(0.030)(0.043)	44	107	1.055(0.043)(0.130)
41	89	0.190(0.002)(0.026)	42	105	0.136(0.023)(0.022)	44	108	0.476(0.032)(0.064)
41	90	0.536(0.005)(0.069)	43	93	0.138(0.002)(0.017)	44	109	0.222(0.024)(0.032)
41	91	1.202(0.009)(0.180)	43	94	0.258(0.003)(0.035)	44	110	0.095(0.018)(0.017)
41	92	2.072(0.018)(0.317)	43	95	0.628(0.006)(0.080)	45	96	0.017(0.001)(0.003)
41	93	3.226(0.035)(0.498)	43	96	1.094(0.011)(0.134)	45	97	0.059(0.001)(0.011)
41	94	3.845(0.041)(0.482)	43	97	1.844(0.020)(0.227)	45	98	0.107(0.002)(0.014)
41	95	4.418(0.046)(0.560)	43	98	2.798(0.034)(0.369)	45	99	0.305(0.004)(0.054)
41	96	4.187(0.047)(0.529)	43	99	3.573(0.038)(0.435)	45	100	0.533(0.007)(0.080)
41	97	3.559(0.051)(0.435)	43	100	3.705(0.040)(0.462)	45	101	1.048(0.014)(0.143)
41	98	2.154(0.051)(0.284)	43	101	3.912(0.049)(0.533)	45	102	1.892(0.024)(0.273)
41	99	1.980(0.081)(0.286)	43	102	3.081(0.053)(0.381)	45	103	2.729(0.031)(0.346)
41	100	0.994(0.050)(0.131)	43	103	2.195(0.086)(0.274)	45	104	3.197(0.035)(0.411)
41	101	0.489(0.038)(0.074)	43	104	1.645(0.061)(0.209)	45	105	3.401(0.039)(0.449)
41	102	0.225(0.027)(0.030)	43	105	0.856(0.043)(0.111)	45	106	3.164(0.045)(0.425)
42	89	0.004(0.000)(0.001)	43	106	0.321(0.027)(0.040)	45	107	2.378(0.047)(0.308)
42	90	0.038(0.001)(0.007)	43	107	0.169(0.023)(0.021)	45	108	1.999(0.079)(0.281)
42	91	0.134(0.002)(0.018)	44	94	0.020(0.001)(0.003)	45	109	1.531(0.056)(0.248)
42	92	0.385(0.004)(0.065)	44	95	0.089(0.002)(0.016)	45	110	0.572(0.032)(0.078)
42	93	0.823(0.008)(0.127)	44	96	0.214(0.003)(0.040)	45	111	0.225(0.022)(0.028)
42	94	1.536(0.016)(0.230)	44	97	0.393(0.005)(0.052)	45	112	0.131(0.020)(0.020)
42	95	2.427(0.026)(0.303)	44	98	0.787(0.010)(0.103)	46	100	0.084(0.002)(0.015)
42	96	3.543(0.038)(0.431)	44	99	1.428(0.019)(0.187)	46	101	0.190(0.003)(0.028)
42	97	4.151(0.042)(0.515)	44	100	2.438(0.029)(0.317)	46	102	0.327(0.005)(0.040)

Table 8

The production cross-sections in millibarns of the measured isotopes, (first column). The second and the third columns represent the statistical and systematical uncertainty, respectively.

Z	A	$\sigma(mb)$	Z	A	$\sigma(mb)$	Z	A	$\sigma(mb)$
46	103	0.672(0.011)(0.096)	48	109	1.060(0.019)(0.143)	50	119	0.877(0.047)(0.114)
46	104	1.289(0.020)(0.157)	48	110	1.577(0.023)(0.206)	50	120	0.756(0.037)(0.102)
46	105	2.121(0.028)(0.309)	48	111	1.863(0.027)(0.247)	50	121	0.421(0.027)(0.077)
46	106	2.805(0.033)(0.393)	48	112	1.963(0.031)(0.266)	51	114	0.141(0.006)(0.021)
46	107	2.977(0.035)(0.409)	48	113	1.962(0.037)(0.265)	51	115	0.269(0.009)(0.046)
46	108	2.914(0.039)(0.371)	48	114	1.330(0.042)(0.169)	51	116	0.409(0.012)(0.052)
46	109	2.351(0.045)(0.324)	48	115	1.264(0.055)(0.180)	51	117	0.629(0.015)(0.078)
46	110	1.980(0.083)(0.295)	48	116	0.877(0.039)(0.150)	51	118	0.796(0.018)(0.123)
46	111	1.361(0.053)(0.217)	48	117	0.399(0.025)(0.055)	51	119	0.886(0.026)(0.128)
46	112	0.633(0.033)(0.083)	48	118	0.178(0.020)(0.028)	51	120	0.826(0.024)(0.112)
46	113	0.299(0.025)(0.038)	49	109	0.201(0.005)(0.036)	51	121	0.814(0.061)(0.126)
46	114	0.130(0.023)(0.016)	49	110	0.401(0.010)(0.053)	51	122	0.659(0.042)(0.110)
46	115	0.082(0.016)(0.010)	49	111	0.716(0.015)(0.116)	51	123	0.375(0.026)(0.051)
47	104	0.232(0.004)(0.030)	49	112	1.008(0.020)(0.127)	51	124	0.212(0.019)(0.034)
47	105	0.494(0.009)(0.063)	49	113	1.401(0.024)(0.196)	51	125	0.111(0.016)(0.016)
47	106	0.934(0.016)(0.141)	49	114	1.656(0.027)(0.296)	52	116	0.087(0.012)(0.013)
47	107	1.457(0.022)(0.192)	49	115	1.530(0.030)(0.195)	52	117	0.150(0.007)(0.020)
47	108	1.903(0.026)(0.239)	49	116	1.239(0.032)(0.184)	52	118	0.303(0.010)(0.059)
47	109	2.319(0.030)(0.296)	49	117	1.121(0.057)(0.155)	52	119	0.432(0.013)(0.069)
47	110	2.476(0.038)(0.399)	49	118	0.799(0.037)(0.109)	52	120	0.534(0.017)(0.078)
47	111	2.598(0.046)(0.543)	49	119	0.384(0.023)(0.048)	52	121	0.619(0.019)(0.088)
47	112	1.500(0.077)(0.185)	49	120	0.201(0.019)(0.027)	52	122	0.707(0.027)(0.109)
47	113	1.384(0.055)(0.190)	49	121	0.108(0.019)(0.015)	52	123	0.481(0.080)(0.060)
47	114	0.762(0.036)(0.095)	50	112	0.229(0.008)(0.041)	52	124	0.532(0.053)(0.114)
47	115	0.368(0.027)(0.048)	50	113	0.449(0.012)(0.065)	52	125	0.367(0.025)(0.053)
47	116	0.181(0.019)(0.026)	50	114	0.726(0.016)(0.102)	52	126	0.198(0.021)(0.031)
47	117	0.096(0.015)(0.012)	50	115	1.039(0.019)(0.174)	52	127	0.091(0.015)(0.014)
48	106	0.188(0.004)(0.033)	50	116	1.148(0.022)(0.167)	52	128	0.052(0.013)(0.007)
48	107	0.307(0.007)(0.044)	50	117	1.131(0.023)(0.142)	52	129	0.060(0.014)(0.012)
48	108	0.659(0.014)(0.103)	50	118	1.018(0.026)(0.127)	53	117	0.014(0.001)(0.002)

Table 9

The production cross-sections in millibars of the measured isotopes, (first column). The second and the third columns represent the statistical and systematical absolute uncertainty, respectively.

Z	A	$\sigma(mb)$	Z	A	$\sigma(mb)$
53	118	0.055(0.008)(0.014)	55	132	0.137(0.029)(0.024)
53	119	0.083(0.007)(0.021)	55	133	0.132(0.016)(0.019)
53	120	0.191(0.008)(0.061)	56	129	0.117(0.007)(0.016)
53	121	0.285(0.012)(0.057)	56	130	0.176(0.013)(0.032)
53	122	0.353(0.012)(0.053)	56	131	0.129(0.018)(0.025)
53	123	0.431(0.017)(0.081)	56	132	0.153(0.017)(0.026)
53	124	0.461(0.023)(0.075)	56	133	0.162(0.073)(0.036)
53	125	0.427(0.037)(0.063)	56	134	0.139(0.019)(0.025)
53	126	0.415(0.048)(0.086)	56	135	0.132(0.020)(0.030)
53	127	0.267(0.025)(0.035)	56	136	0.103(0.017)(0.014)
53	128	0.177(0.018)(0.031)			
53	129	0.104(0.018)(0.018)			
54	122	0.097(0.006)(0.017)			
54	123	0.153(0.007)(0.020)			
54	124	0.233(0.010)(0.037)			
54	125	0.325(0.022)(0.073)			
54	126	0.337(0.022)(0.061)			
54	127	0.279(0.018)(0.036)			
54	128	0.311(0.042)(0.049)			
54	129	0.293(0.031)(0.071)			
54	130	0.189(0.020)(0.026)			
54	131	0.112(0.017)(0.018)			
54	132	0.082(0.014)(0.013)			
54	133	0.075(0.012)(0.010)			
55	126	0.147(0.011)(0.022)			
55	127	0.172(0.012)(0.039)			
55	128	0.268(0.017)(0.073)			
55	129	0.232(0.054)(0.029)			
55	131	0.212(0.030)(0.044)			

Table 10

The production cross-sections in millibars of the measured isotopes, (first column). The second and the third columns represent the statistical and systematical absolute uncertainty, respectively.

Z	$v_{cm}(cm/ns)$	δv_{cm}	Z	$v_{cm}(cm/ns)$	δv_{cm}
23	1.71	0.02	42	1.10	0.02
24	1.66	0.03	43	1.07	0.02
25	1.65	0.03	44	1.04	0.02
26	1.58	0.02	45	1.02	0.02
27	1.57	0.02	46	0.99	0.04
28	1.52	0.03	47	0.96	0.04
29	1.50	0.01	48	0.92	0.02
30	1.48	0.04	49	0.89	0.02
31	1.42	0.03	50	0.86	0.02
32	1.40	0.04	51	0.83	0.02
33	1.36	0.02	52	0.80	0.03
34	1.34	0.03	53	0.78	0.03
35	1.31	0.03	54	0.75	0.02
36	1.28	0.02	55	0.72	0.02
37	1.26	0.04	56	0.71	0.03
38	1.22	0.04			
39	1.20	0.04			
40	1.15	0.03			
41	1.13	0.03			

Table 11
Mean velocity values corrected for the angular acceptance for each fission element. The third column represents the standard deviation of all isotopes with a given charge value.